

Vertical beam size measurement in the CESR-TA e^+e^- storage ring using x-rays from synchrotron radiation

J. P. Alexander, A. Chatterjee, C. Conolly, E. Edwards, M. P. Ehrlichman, E. Fontes, B. K. Heltsley*, W. Hopkins¹, A. Lyndaker, D. P. Peterson, N. T. Rider, D. L. Rubin, J. Savino², R. Seeley, and, J. Shanks

Cornell University, Ithaca, NY 14853, USA

J. W. Flanagan

High Energy Accelerator Research Organization (KEK), Tsukuba, Japan

Abstract

We describe the construction and operation of an x-ray beam size monitor (xBSM), a device measuring e^+ and e^- beam sizes in the CESR-TA storage ring using synchrotron radiation. The device can measure vertical beam sizes of 10 – 100 μm on a turn-by-turn, bunch-by-bunch basis at e^\pm beam energies of ~ 2 GeV. At such beam energies the xBSM images x-rays of $\epsilon \approx 1\text{-}10$ keV ($\lambda \approx 0.1 - 1$ nm) that emerge from a hard-bend magnet through a single- or multiple-slit (coded aperture) optical element onto an array of 32 InGaAs photodiodes with 50 μm pitch. Beamlines and detectors are entirely in-vacuum, enabling single-shot beam size measurement down to below 0.1 mA (2.5×10^9 particles) per bunch and inter-bunch spacing of as little as 4 ns. At $E_b = 2.1$ GeV, systematic precision of ~ 1 μm is achieved for a beam size of ~ 12 μm ; this is expected to scale as $\propto 1/\sigma_b$ and $\propto 1/E_b$. Achieving this precision requires comprehensive alignment and calibration of the detector, optical elements, and x-ray beam. Data from the xBSM have been used to extract characteristics of beam oscillations on long and short timescales, and to make detailed studies of low-emittance tuning, intra-beam scattering, electron cloud effects, and multi-bunch instabilities.

Keywords: electron beam size, x-ray diffraction, pinhole, coded aperture, synchrotron radiation, electron storage ring

Contents

1	Introduction	2			
2	Methods & tools	2			
2.1	X-ray spectrum	2			
2.2	Point response function	3			
2.3	Image processing	6			
2.4	Software tools	6			
2.4.1	PRF generation	6			
2.4.2	Data processing	7			
2.5	Optical element design	7			
3	Apparatus	10			
3.1	Beamline	11			
3.2	Detector	11			
3.3	Optical elements	13			
3.4	Readout & data acquisition	15			
4	Operations	17			
4.1	Installation	17			
4.2	Detector & Optic Alignment	17			
4.3	Beam-induced coded aperture damage	19			
			4.4	Calibrations	19
			4.5	Setting the pinhole opening	21
			5	Results	21
			5.1	Detector spectral response	21
			5.2	Beam size extraction	24
			5.3	Optical element models	25
			5.4	Systematic uncertainty in beam size	27
			5.4.1	Magnification	28
			5.4.2	Pinhole lip width	28
			5.4.3	Pinhole gap opening	28
			5.4.4	Coded aperture slit size	29
			5.4.5	Coded aperture masking thickness	29
			5.4.6	Misaligned optical element	29
			5.4.7	Spectral sensitivity	30
			5.4.8	Data-to-data comparisons	31
			5.4.9	Summary	32
			5.5	Bunch Oscillations	32
			5.6	Multi-bunch performance	33
			6	Conclusions	33

*Corresponding author

Email address: bkh2@cornell.edu (B. K. Heltsley)

¹Current address: Department of Physics, University of Oregon, Eugene, OR 97403, USA

²Current address: National Superconducting Cyclotron Laboratory, Michigan State University, East Lansing, MI 48824, USA

1. Introduction

Precision measurement of vertical bunch size plays an increasingly important role [1] in the design and operation of the current and future generation of electron storage rings. Such facilities include an e^+e^- collider (Super-KEKB [2]), an e^- -ion collider (EIC [3]), a multitude of present and future light sources [4, 5] (e.g., PEPLS [6]), and a positron damping ring for an e^+e^- linear collider (ILC [7] or CLIC [8]). For each of these machines, performance (e.g., luminosity or brightness) is directly related to the vertical emittance (and thus the vertical beam size). By providing the operator with real-time vertical beam size information, the accelerator can be tuned in a predictable, stable, and robust manner. Optical transition radiation [9, 10], optical diffraction radiation [11–13], and synchrotron radiation imaging have been successfully used for such measurements using a variety of techniques. Synchrotron radiation can be used in the visible with a streak camera [14], an interferometer [15–17], or a vertical polarization monitor [18]; x-rays can be used with a pinhole camera [19–21], refractive lenses [22], Fresnel zone plates [23–25], or a Bragg polarimeter [26]. Challenges persist in obtaining precision at low beam size and current, as well as ability to distinguish among closely spaced bunches in extended trains, for which electron cloud effects can be large.

In 2008 the Cornell Electron Storage Ring (CESR) was re-configured as a Test Accelerator (CESR-TA [27]) with the intent of studying electron and positron beam dynamics. Parameters for the CESR storage ring are shown in Table 1. The CESR storage ring is uniquely equipped for examining single-beam phenomena limiting the performance of next-generation colliders and storage rings. As a former collider which operated in both the $c\bar{c}$ and $b\bar{b}$ threshold regions, CESR is able to circulate either electrons or positrons, and to do so with beam energies from 1.5-5.3 GeV, enabling controlled measurements of charge- and energy-dependence.

Table 1: Parameters of the Cornell Electron Storage Ring Test Accelerator (CESR-TA).

Parameter	Value
Circumference	768.4 m
Circulation Time	2.563 μ s
Circulation Frequency	390.1 kHz
Beam Energy	2.085 (1.5-5.3) GeV
Species	e^+ or e^-
RF Frequency	500 MHz
Harmonic Number	1281
Bunch Spacing	≥ 4 ns
Bunch Population	$0.1\text{-}10 \times 10^{10}$
Number of Bunches/Turn	≤ 45
Horizontal emittance	2.6 nm
Vertical emittance	≥ 10 pm
Longitudinal bunch size (rms)	10-15 mm
Horizontal bunch size (rms)	170-300 μ m
Vertical bunch size (rms)	10-100 μ m

One component of the CESR-TA program is the xBSM (x-ray Beam Size Monitor). The desired specifications on vertical beam size instrumentation pose significant technical challenges: attaining sensitivity to beam size at the $\sim 10\text{-}100$ μ m level with precision at the few μ m level; bunch-by-bunch, turn-by-turn measurements on a train of bunches with inter-bunch spacing of 4 ns; single-shot operation for 0.1-10 mA bunch current; and fast feedback on beam size measurement to facilitate real-time tuning. This article describes the xBSM conceptual basics and data analysis methods in Sect. 2, apparatus in Sect. 3, operational procedures and experience in Sect. 4, measurement capabilities in Sect. 5, and important conclusions in Sect. 6.

2. Methods & tools

Each xBSM installation images x-rays from a hard-bend magnet through a single- or multiple-slit optical element³ onto a detector, a 32-pixel array of photodiodes read out with fast electronics. Before describing the apparatus in detail in Sect. 3, this section will review the conceptual basis of the device, with particular attention to design principles and tools as well as analysis techniques.

2.1. X-ray spectrum

The design and performance of optical and detector elements depend strongly upon the x-ray spectrum. Here we review the formalism relevant to synchrotron radiation. The radiated power spectrum of a charged particle in a uniform magnetic field is given by the well-known formulae developed by Larmor [28], Liénard [29], Wiechert [30], and, most prominently, Schott [31], which were later summarized in modern form by Schwinger [32] and Jackson [33]. The synchrotron radiation spectrum is a direct function of beam energy E_b , angle θ out of the orbital plane, instantaneous magnetic bend radius ρ , and photon energy $\epsilon \equiv \hbar\omega = hc/\lambda$, where h (\hbar) is the (reduced) Planck constant, ω is the radial frequency, λ is the wavelength, and c is the speed of light.

We define the Lorentz factor γ , the wave number k , the peak of the incident power spectrum ϵ_c (also known as the critical energy⁴), and a useful dimensionless quantity ξ as

$$\begin{aligned} \gamma &\equiv \frac{E_b}{m_e c^2}, \\ k &\equiv \frac{2\pi}{\lambda} = \frac{\epsilon}{\hbar c}, \\ \epsilon_c &\equiv \gamma^3 \frac{3\hbar c}{2\rho}, \text{ and} \\ \xi &\equiv \frac{\epsilon}{2\epsilon_c} (1 + \gamma^2 \theta^2)^{\frac{3}{2}}, \end{aligned} \quad (1)$$

where m_e is the electron mass. Then the complex amplitude can be written as

$$\mathbf{E}_{\text{syn}}(r, \epsilon, \theta; \gamma, \rho) = \frac{e^{ikr}}{\sqrt{r}} (E_{\parallel} \hat{\mathbf{u}}_{\parallel} + E_{\perp} \hat{\mathbf{u}}_{\perp}) \quad (2)$$

³We refer to a single slit optical element as a *pinhole* (PH) and multiple-slit element as *coded aperture* (CA).

⁴The definition of the critical energy ϵ_c used here is half that of Jackson [33].

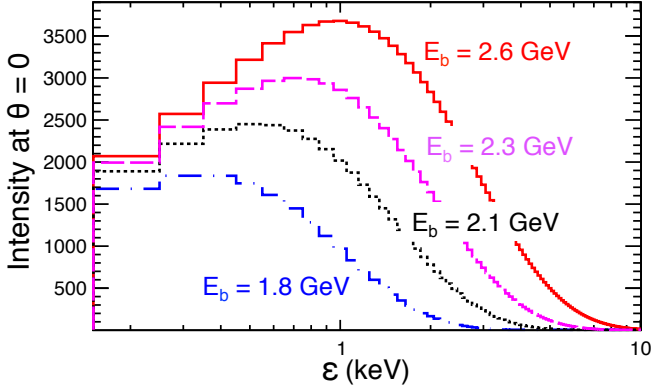


Figure 1: X-ray intensity spectrum (in arbitrary units) from synchrotron radiation incident on the CESR-TA xBSM optical element at $\theta = 0$ for several e^\pm beam energies used at CESR-TA, using Eq. (3).

and the differential radiated power as

$$\frac{d^2W}{d\theta d\epsilon}(\epsilon, \theta) = |E_{\parallel} \hat{\mathbf{u}}_{\parallel} + E_{\perp} \hat{\mathbf{u}}_{\perp}|^2, \quad (3)$$

where r is the two-dimensional distance from the emission point, and $\hat{\mathbf{u}}_{\parallel}$ and $\hat{\mathbf{u}}_{\perp}$ are orthogonal polarization unit vectors into and out of the plane of motion, respectively. The coefficients of the two orthogonal components of the amplitude are given by

$$\begin{aligned} E_{\parallel} &\equiv E_0 K_{2/3}(\xi) \text{ and} \\ E_{\perp} &\equiv E_0 K_{1/3}(\xi) \frac{\gamma\theta}{\sqrt{1+\gamma^2\theta^2}}, \text{ where} \\ E_0 &\equiv \frac{\epsilon}{\epsilon_c} \gamma (1+\gamma^2\theta^2) \sqrt{\frac{3\alpha}{4\pi^2}}, \end{aligned} \quad (4)$$

The K_ν are modified Bessel functions of the second kind, and α is the fine structure constant. The second term, E_{\perp} , vanishes at $\theta = 0$, and remains small for $\gamma\theta \ll 1$. The angle in the horizontal plane has already been integrated out in Eq. (2), which can be justified by noting that for the dimensions of the apparatus used here and the relevant wavelengths, the horizontal and vertical contributions to pathlength are decoupled. Hence the radial dependence of the amplitude is $1/\sqrt{r}$, appropriate for radiation in two dimensions, rather than the usual $1/r$ dependence for a spherical wave.

Table 2: Parameters defining the CESR xBSM x-ray spectrum. The critical energy ϵ_c is defined in Eq. (1), and σ_θ in Eq. (6).

E_b (GeV)	ϵ_c (keV)	$\sigma_\theta(3 \text{ keV})$ (μrad)
1.811 (“1.8”)	0.416	61
2.085 (“2.1”)	0.634	65
2.305 (“2.3”)	0.858	68
2.553 (“2.6”)	1.166	72

For CESR-TA, the hard-bend magnet at the xBSM source point has $\rho = 31.65$ m. Table 2 shows the critical energies and

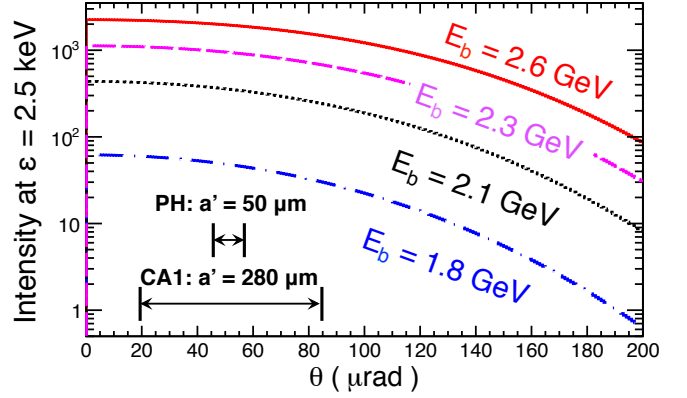


Figure 2: X-ray intensity from Eq. (3) (in arbitrary units) vs. vertical angle θ at $\epsilon = 2.5$ keV for synchrotron radiation at several e^\pm beam energies used at CESR-TA. Two (uncentered) spans are indicated, one each for pinhole (PH) and coded aperture (CA1) optical elements (see Table 4); nominally these should be centered on $\theta = 0$.

Fig. 1 shows Eq. (3) evaluated at $\theta = 0$ for the four e^\pm beam energies from 1.8 to 2.6 GeV which were used to characterize xBSM performance; ϵ_c ranges from ~ 0.4 -1.2 keV. Most of the detected x-ray intensity lies in the range $1 < \epsilon/\epsilon_c < 10$. Over this range one can approximate [33] the differential radiated power near $\theta = 0$ as

$$\begin{aligned} \frac{dW}{d\theta} &= r |\mathbf{E}_{\text{syn}}(\epsilon > \epsilon_c, \theta = 0; \gamma, \rho)|^2 \\ &\approx \frac{10}{3} \gamma^2 \frac{\epsilon}{\epsilon_c} e^{-\epsilon/\epsilon_c}, \end{aligned} \quad (5)$$

which monotonically decreases by a factor of ~ 1000 over the range $\epsilon/\epsilon_c = 1 - 10$. Eq. (5) gives a value ~ 15 -20% smaller than Eq. (2) at $\epsilon/\epsilon_c = 1$ but converges to it as ϵ/ϵ_c increases.

For $\epsilon > \epsilon_c$, the angular dependence of the radiated power is approximately Gaussian with width

$$\sigma_\theta \equiv \frac{1}{\gamma} \sqrt{\frac{\epsilon_c}{3\epsilon}} = \sqrt{\frac{\gamma \hbar c}{2 \rho \epsilon}}. \quad (6)$$

For $E_b = 2.6$ GeV and $\epsilon = 3\epsilon_c$, $\theta_c = 60 \mu\text{rad}$, which is nearly double the maximum allowed ($\sim 35 \mu\text{rad}$ for an optical element centered on the beam) by the xBSM optics (apertures of 50-300 μm), for a beam vertically centered on the optical element. As shown in Fig. 2, variation of radiated power with vertical angle is modest but not negligible at CESR-TA, falling by $\sim 10\%$ (or less, depending on the optical element and beam energy) from the center to the edge of the images.

2.2. Point response function

After passing through an optical element, x-rays from a point source form a diffraction pattern with single or multiple prominent peaks on the pixel detector. This pattern is the *point response function* (prf) $\mathcal{F}(y)$, the expected x-ray intensity distribution at the image plane for zero beam size and a given

Table 3: Geometrical parameters defining the CESR-TA xBSM beamlines. Geometrical quantities are defined in Fig. 3. Distances assume the coded aperture optic; the pinhole optic is 25 mm closer to the source point and hence has a magnification value about 1% larger than shown. The uncertainties on L are from an optical survey; on L' from the survey, known CESR orbit, and associated depth of field.

Parameter	e^- beamline	e^+ beamline
L	4356.5 ± 3.9 mm	4485.2 ± 4.0 mm
L'	10621.1 ± 1.0 mm	10011.7 ± 1.0 mm
$M \equiv L'/L$	2.4380 ± 0.0022	2.2322 ± 0.0020
a'	$\approx 50 - 300$ μm	same as e^-
a	$\approx 50 - 1000$ μm	same as e^-
$2\theta_{\text{max}} = a'/L$	$11 - 69$ μrad	$11 - 67$ μrad

x-ray spectrum, beam line geometry, optical element, and filter in front of the detector. A simplified schematic of the geometry is shown in Fig. 3, and the gross dimensions in Table 3. A non-zero vertical beam size creates an image with broader peaks than that of a point source because the image is a weighted superposition due to a continuum of vertically offset point sources. Extracting the vertical beam size from image data requires knowledge of the prf.

Diffraction of light from a point source through an optical element to an image plane, with geometry as shown in Fig. 3, can be described by the Fresnel-Kirchoff formula [33], which expresses the complex amplitude for the wavefront at the image plane as an integral over the optical element footprint. Simplifying the general formula to that of a one-dimensional optic and

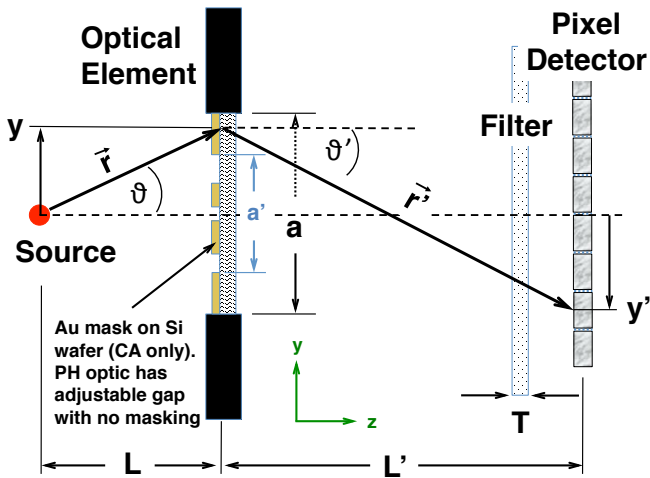


Figure 3: Simplified schematic of xBSM layout (not to scale). The distinction between a and a' is that a is the total vertical extent of partial transmission through the mask material, and a' is the vertical extent of features (slits) in the mask; for the pinhole (PH) optic, which has no masking, $a = a'$.

image, we obtain:

$$\mathbf{E}_{\text{img}}(y', \epsilon) = -i\sqrt{k} \int_{-a/2}^{+a/2} (E_{\parallel} \hat{\mathbf{u}}_{\parallel} + E_{\perp} \hat{\mathbf{u}}_{\perp}) \times \frac{e^{ik(r+r'+(n-1)T)}}{\sqrt{rr'}} \times \frac{\cos \theta + \cos \theta'}{2} dy \quad (7)$$

where a , r , r' , θ , and θ' are defined in Fig. 3; E_{\parallel} and E_{\perp} are given by Eq. (4) and depend upon θ and therefore on y ; n is the (complex) index of refraction, which contains effects of any partially opaque materials blocking the aperture, both a phase shift (real) and absorption (imaginary), which have y and λ dependences; and T is the material thickness (which may also vary with y).

Because x-ray wavelengths are small compared to aperture sizes and both source-optic and optic-image separations, further simplifications are possible. Typical apertures at CESR-TA range from 50-300 μm , distances from 4-10 m, and wavelengths from 0.1-1 nm. Image offsets y' are less than 1 mm. These parameter values result in the well-known diffraction figure of merit $a^2/(L'\lambda) \approx 1$; this value is not small enough for a far-field (Fraunhofer diffraction) approximation, but appropriate for the near-field (Fresnel) diffraction.

We approximate the source as a vertical line, with no horizontal or longitudinal extent. Both bunch and detector dimensions (Tables 1 and 5) are very small compared to L and L' , resulting in the magnification $M \equiv L'/L$ being nearly constant over the bunch volume, justifying the approximation.

In Fresnel diffraction, the wavefronts must be considered as cylindrical for a one-dimensional optic, not planar, and the image remains sensitive to the optic-image separation. Assuming the source is located at $y = 0$,

$$\begin{aligned} \cos \theta &\approx 1, \\ \cos \theta' &\approx 1, \\ r + r' &\approx L + L' + \frac{y^2}{2L} + \frac{(y' - y)^2}{2L'}, \\ r r' &\approx LL', \end{aligned} \quad (8)$$

which lead to

$$\mathbf{E}_{\text{img}}(y', \epsilon) = -i\sqrt{k} \frac{e^{ik(L+L')}}{\sqrt{LL'}} \times \int_{-a/2}^{+a/2} (E_{\parallel} \hat{\mathbf{u}}_{\parallel} + E_{\perp} \hat{\mathbf{u}}_{\perp}) \times \exp \left[ik \left(\frac{y^2}{2L} + \frac{(y' - y)^2}{2L'} + (n-1)T \right) \right] dy; \quad (9)$$

i.e., for a wave number k , the complex amplitude at any point y' on the image plane is calculated by integrating over the aperture, accounting at each point y for the synchrotron radiation amplitude in the absence of the optic, the relative phase advance at that wavelength due to both path length and material, and the attenuation of intensity due to distance traveled and material traversed. The prf is then obtained by integrating over all

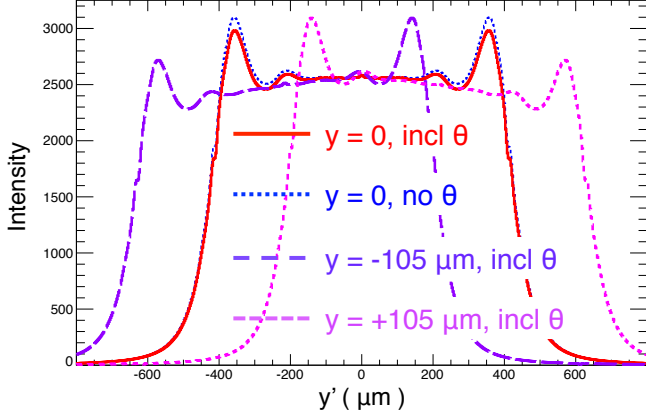


Figure 4: Predicted point response functions for a 300 μm pinhole optic at $E_b = 2.1$ GeV. As indicated, the curves correspond to the source point being centered on the slit or offset from center, either including or not including dependence of the synchrotron radiation intensity on the vertical angle θ out of the bend plane.

wavelengths (energies):

$$\mathcal{F}(y') \equiv \int_0^{+\infty} \mathcal{S}_d(\epsilon) \mathcal{S}_f(\epsilon) \left| \mathbf{E}_{\text{img}}(y', \epsilon) \right|^2 d\epsilon. \quad (10)$$

where $\mathcal{S}_d(\epsilon)$ specifies the spectral response of the detector, empirically determined in Sect. 5.1, and $\mathcal{S}_f(\epsilon)$ the spectral response of whatever partially transmitting material are present in the filter and optical element. Accounting for the effects of materials in the path of the x-rays is straightforward; however, one must account for the y -dependence of T and the λ dependence of n . Designating each traversed material by the subscript m , the complex index of refraction term is

$$(n - 1)T \equiv \lambda^2 \frac{r_e N_A}{2\pi} \sum_m \frac{\rho_m T_m}{A_m} \left[f_1^m(\lambda) + i f_2^m(\lambda) \right], \quad (11)$$

where r_e is the electron radius, N_A is Avogadro's number, ρ_m is the density of material m , A_m is the atomic number of material m , and f_1 and f_2 are the *atomic scattering factors* tabulated [34] as functions of x-ray energy. The factor f_2 accounts for absorption of x-rays, and can have both smoothly varying energy dependence and abrupt, discontinuous spikes in transmission corresponding to the various atomic shell energies.

It should be noted that Eq. (10) implicitly assumes that the source point is vertically centered on the optical element. Generally this is not the case, and it matters because of the θ -dependence of Eq. (2). Figure 4 shows⁵ how θ -dependence and beam position offset affect the box-like prf for a wide-slit pinhole optic. Note that when the distribution shifts due to a beam position offset, it is also slightly distorted relative to the shape with no offset. While this dependence can be accommodated exactly, it is computationally cumbersome to do so relative to what can be accomplished using a factorization approximation

⁵Figure 4 and all subsequent figures displaying a quantity dependent upon the x-ray spectrum (such as a prf) apply the measured spectral response of the detector described in Sect. 5.1 and effect of filters and materials in the x-ray beam using Eq. (11) and the atomic scattering factors of [34].

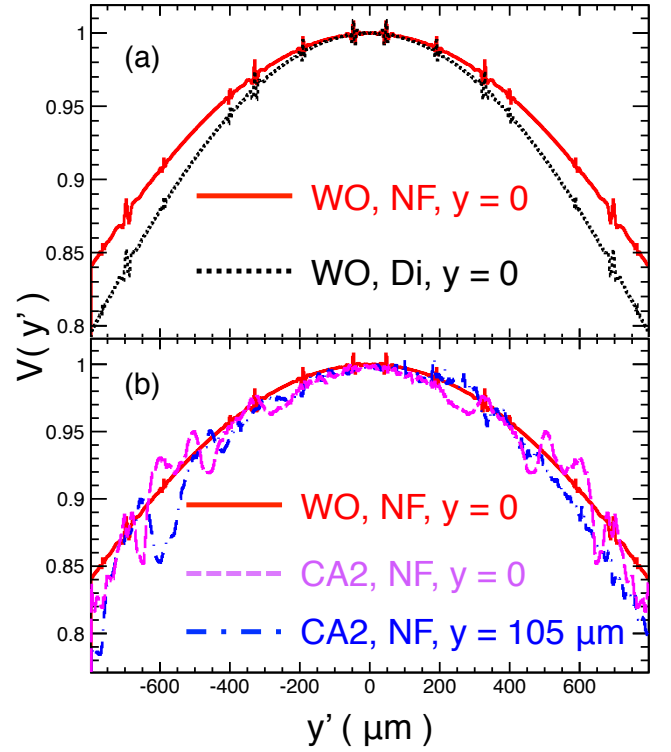


Figure 5: The angular correction function $\mathcal{V}(y')$ (see Eq. (12)) at $E_b = 2.1$ GeV for different combinations of an optical element and filter with vertical beam offsets. Optical elements (WO and CA2) are described in Table 4 and filters (NF and Di) in Table 6. The small and narrow ($\text{fwhm} \approx 10 \mu\text{m}$) spikes in the WO-optic curves, which are expected to be smooth, are artifacts of the numerical approximations; broad ($\text{fwhm} > 20 \mu\text{m}$) features are due to interference.

on the prf for beam position $y_b \neq 0$. To first order, the prf can be expressed as the product of two functions, one assuming a vertical beam profile that is uniform in y_b , and the second that imposes the vertical envelope of the synchrotron radiation field, which might not be centered on the optical element. This second function we designate as $\mathcal{V}(y')$, which is the ratio of Eq. (10) evaluated for a given optical element to that evaluated with vertical angle $\theta \equiv 0$ for the same optical element. (For pinholes, $\mathcal{V}(y')$ is obtained from a wide-open optical element, whereas for coded apertures (CA), where there is at least partial transmission to the entire detector, $\mathcal{V}(y')$ is obtained for the CA itself.) By construction, $\mathcal{V}(0) = 1$, $\mathcal{V}(y') = \mathcal{V}(-y')$, $\mathcal{V}(y')$ is concave-down, and $\mathcal{G}(y', y_b)$ is exact for the trivial case of a wide-open optical element. Figs. 5(a) and (b) show $\mathcal{V}(y')$ for a wide-open optic and a coded aperture; the curve for the diamond filter (relative to none) accounts for the stiffer spectrum with correspondingly steeper y' -dependence. Thus, the prf for $y_b \neq 0$ is

$$\mathcal{G}(y', y_b) \approx \frac{\mathcal{F}(y' + My_b)}{\mathcal{V}(y' + My_b)} \times \mathcal{V}(y' - y_b) \quad (12)$$

where $M \equiv L'/L$ is the *magnification* (the ratio of the optic-image separation to source-optic distance), the first term is the y_b -independent prf, and the second imposes the vertical beam

profile. For any pinhole optic with opening $\sim 50 \mu\text{m}$, the approximation is essentially exact for beam offsets up to $\sim 200 \mu\text{m}$. The approximation in Eq. (12) is exact for $y_b=0$, and can be seen in Fig. 5(b) to be valid for a coded aperture to within a few percent rms for beam energies and beam offsets encountered at CESR-TA. The importance and usefulness of accounting for $y_b \neq 0$ is demonstrated in Sect. 5.4.6.

2.3. Image processing

Once the prf $\mathcal{F}(y')$ is in hand, each measured image can be fit for the beam size, beam position, and intensity that minimize χ^2 between data points and the smeared, offset, and amplified prf, assuming a Gaussian beam profile and incoherent radiation from different vertical slices of the bunch. Vertical beam position and detector offset for any given image are highly anti-correlated, so typically the detector is centered during instrument setup; however the formalism below includes detector offset, with the understanding that it cannot vary from one turn or bunch to the next in a given dataset. The fitting function $\mathcal{H}(y'; A_b, \sigma_b, y_b, d)$ has dependent variable y' and four parameters [beam intensity (A_b), vertical beam size (σ_b), vertical beam offset from the center of the optic (y_b), and vertical offset of the center of the detector from the center of the optic (d)]:

$$\mathcal{H}(y'; A_b, \sigma_b, y_b, d) \equiv \frac{A_b \hat{\mathcal{H}}(y' - My_b - d; \sigma_b, y_b)}{\int_{-\infty}^{+\infty} d\eta \int_0^{+\infty} dk |\mathbf{E}(\eta, k)|^2} \quad (13)$$

where

$$\hat{\mathcal{H}}(y'; \sigma_b, y_b) \equiv \frac{1}{\sigma_b \sqrt{2\pi}} \times \int_{-\infty}^{+\infty} \exp\left[-\frac{1}{2} \left(\frac{y' - \eta}{M\sigma_b}\right)^2\right] \times \mathcal{G}(y' - \eta, y_b + \eta/M) d\eta \quad (14)$$

and η is an integration variable of the vertical coordinate at the image plane. The fitting function convolves a Gaussian shape approximating the beam profile with the prf, translates it in the vertical dimension and amplifies it, thus extracting a best-fit beam size, beam position, and intensity of light incident on the detector. The centered and smeared intermediate function, $\hat{\mathcal{H}}(y'; \sigma_b, y_b)$, is computed from $\mathcal{F}(\eta)$ by numerical integration for a discrete set of evenly spaced beam sizes $\sigma_{bj} \equiv j \times \Delta\sigma_b$, $j = 0, 1, 2, \dots$, and source positions $y_{bk} \equiv \pm k \times \Delta y_b$, $k = 0, 1, 2, \dots$, with values at intermediate beam sizes obtained from linear interpolation between the two nearest σ_{bj} or y_{bk} , respectively. For our purposes we have found that there are no changes in results for $\Delta\sigma_b$ below $2 \mu\text{m}$ or $\Delta y_b = 10 \mu\text{m}$, and therefore use those values. The discrete set of templates $\hat{\mathcal{H}}_{jk}(y') \equiv \hat{\mathcal{H}}(y'; \sigma_{bj}, y_{bk})$ need only be computed once, stored in files, and then be read into memory for use in image fitting.

2.4. Software tools

Two general classes of software tools have been developed: one that generates a point response function, and one that processes xBSM data. The former class implements the optical element formalism of Sect. 2.1 and 2.2, numerically implementing

Eq. (10) using the known characteristics of the beam, bending magnet, beamline geometry, optical elements, filters, and detector spectral response, and the latter subsumes all calibration, diagnostic, and analysis functions. PRF generation is implemented in a C++ program using the CERN ROOT [35] package for diagnostic plots; an EXCEL® version using more approximations is used for real-time feedback and online analysis. Two sets of code for data processing are maintained, one using MATLAB® [36] for online data acquisition, alignment, and diagnostics during setup, and a second in C++/ROOT for more refined analysis.

2.4.1. PRF generation

For each combination of beam energy, optical element, filter, and geometrical layout, a separate prf is needed because it depends critically on the geometry and the x-ray spectrum. A prf consists of a list of $[y', \mathcal{F}(y'), \mathcal{V}(y')]$ triplets at evenly spaced y' intervals covering not only the detector height but enough beyond the detector edge to accommodate possible beam motion of up to $\sim 400 \mu\text{m}$. For each point, the integrals of Eq. (9) and Eq. (10) must be performed. These proceed as follows:

- Parameters specifying the geometry, beam energy, bend radius, optical element pattern, integration step sizes, mask and filter materials and thicknesses, detector spectral response, etc., are assembled in a text *settings file* in which each parameter is identified by name and followed by its value.
- A complex amplitude is accumulated at points on the image plane separated by $dy' = 2.5 \mu\text{m}$ for $y' \in [-2000, 2000] \mu\text{m}$; each is initialized to zero for each x-ray energy ϵ and suitably incremented for each optic position y .
- The integration of Eq. (9) is performed as a rectangle-rule sum taken in steps of $dy = 0.1 \mu\text{m}$ over all slits and masking strips of the optical element and at least $500 \mu\text{m}$ beyond the extreme slits at each end to include effects of continuous partially transmitting masking material. The atomic scattering factors of [34] are used for evaluation of Eq. (11).
- The integration of Eq. (10) is performed as a simple sum in steps of $d\epsilon = 0.1 \text{ keV}$ in $\epsilon \in [0, 20] \text{ keV}$, weighting each entry by the detector spectral response $\mathcal{S}_d(\epsilon)$, measured in Sect. 5.1 (except, of course, during the procedures of Sect. 5.1, where $\mathcal{S}_d(\epsilon) \equiv 1$).
- The angular correction function $\mathcal{V}(y')$ is computed using the optical element itself, except for a pinhole optic, for which a wide-open optical element is used.

For each of our coded apertures, prf generation requires ~ 20 minutes of single-threaded CPU time on an Intel® Xeon® CPU X5550 @ 2.67GHz (SPECint_base2006 33, SPECfp_base2006 38).

2.4.2. Data processing

Both MATLAB® and C++/ROOT data processing codes perform similar basic functions:

- Read in the data text file, storing and making available the general run information such as run number, beam current, beam energy, CESR bunch structure, pedestals, gains, range, optical element and filter selections, etc. as well as the digitized pulse height for all detector channels for all bunches and all turns in a fixed ordering.
- Correct digitized data for individual channel pedestals and gains, amplifier range, and bunch-to-bunch crosstalk (see Sect. 4.4).
- Define and fill image plots.
- Fit a selection (*e.g.*, first hundred turns, every third turn, all turns, all bunches) of images to an appropriate `prf` for running conditions for up to six parameters: beam size, beam vertical position, intensity, an image component flat across the detector, magnification scaling, and a detector offset d (see Eq. (13)). Generally only the first four parameters are floating and the last two are fixed to 1.0 and 0.0, respectively. The flat component accounts for as much as $\pm 10\%$ percent of the image area⁶ and thought to be due to shifts in electronics response that are coherent across the detector. Magnification scaling is only used to verify the validity of the distance ratios (see Sect. 5.4.1). The value of d is set to a nonzero value only for coded aperture data seen to be misaligned (see Sect. 5.4.6).
- Prevent fitting if the area of the image is below a threshold because in multi-bunch running it sometimes happens that some bunches are read out but are empty of current.
- Calculate turn-averaged quantities of fit parameters for each bunch, preventing bad-fit or no-fit non-statistical outliers from having undue weight.
- As an alternate beam size measurement, construct and fit the sum of all turns for each bunch to the `prf`, which includes beam motion effects but is nevertheless useful for comparison.
- Store useful diagnostic plots and a summary of fit results as text. If the run was taken for calibration purposes, store calibration results appropriately.

The MATLAB® programs are essential for alignment procedures and feedback on the functioning of the electronics and proper filter and optical element selection, all of which must be verified prior to taking production data. However, to get quick feedback, generally only a small fraction of the data are examined (*e.g.*, 100 turns), or images from all turns are summed prior to being fit, because our MATLAB® tool cannot handle the load

of fitting all turns individually in a reasonable time. In addition, `prfs` in the MATLAB® program are limited to multiple-Gaussian approximations to the binned `prfs` from the EXCEL® tool mentioned earlier; template generation and template use are only implemented in the C++/ROOT-based code.

The C++/ROOT program is independently coded and performs all the above functions, but has more flexibility. Specifications on desired analysis are made in text *settings files*, including which bunches and turns are to be fit, fitting options (which parameters are floating or fixed), the `prf` to be fit, etc. Furthermore, more diagnostic information is created, such as two-dimensional plots of fit parameter value vs. beam current (or run number) and bunch number. Running it creates a text output summary `.out` file and a binary `.root` file, the latter of which stores plots, which can be viewed, manipulated, and extracted with the interactive ROOT object browser. The `prf` can be specified as a multi-Gaussian function (for direct comparison with the MATLAB® fits) or a binned version as described in Sect. 2.4.1.

In addition, the C++/ROOT analysis converts three of the fit parameter variations in the time domain (turn number, each turn corresponding to $\sim 2.5 \mu\text{sec}$) into the frequency domain using a discrete fast Fourier transform (FFT), computed using FFTW [37]. Resonances show up at frequencies of characteristic oscillations (such as horizontal and vertical tunes of the storage ring, which can vary slowly with time), or low frequencies associated with A/C line voltage and power supplies.

To perform all the above functions, the C++/ROOT data analysis program requires ~ 7 msec per bunch per turn of single-threaded CPU time on an Intel® Xeon® CPU X5550 @ 2.67GHz (SPECint_base2006 33, SPECfp_base2006 38). The time is dominated by the χ^2 -minimization fitting inside ROOT's MINUIT [38] package.

2.5. Optical element design

Optical elements used at CESR-TA are listed in Table 4, and include WO (wide-open), an adjustable vertical pinhole (PH), and two coded apertures (CA1 and CA2). In this section we discuss characteristics of each and relevant design considerations.

Design and quantitative evaluation of optical elements requires a figure of merit for beam-size resolving power. For the moment, we restrict ourselves to an idealized quantity wherein systematic effects involved in reconstructing beam size are ignored, so that the resulting function $Q(\sigma_b)$ expresses the statistical power of a particular optical element at beam size σ_b . We form a χ^2 -like quantity based on the fact that the pulse height in each of the 32 pixels is proportional to the number of photoelectrons collected there and which will fluctuate according to counting statistics. Pixelizing the kernel of the point response function $\hat{\mathcal{H}}(y'; \sigma_b, y_b)$ defined in Eq. (14):

$$\mathcal{P}_j(\sigma_b) \equiv \int_{\text{pixel } j} \hat{\mathcal{H}}(y'; \sigma_b, y_b) dy' \quad (15)$$

⁶We take *image area* to mean *image intensity summed over all 32 detector channels*.

Table 4: CESR-TA xBSM optic element parameters. Geometrical quantities are defined in Fig. 3. Coded aperture patterns are shown in Fig. 18.

Category	Parameter	Value
WO (wide-open)	$a' \equiv a$	40 mm
PH (pinhole)	Tungsten blade T	2.5 mm
	Downstream taper	2°
	a	0-200 μm
	a'	$\equiv a$
CA1 (coded aperture)	Si T	2.5 μm
	Au T (2 chips)	$0.54 \pm 0.05 \mu\text{m}$
	Au T (2 chips)	$0.69 \pm 0.05 \mu\text{m}$
	a	1000 μm
	a'	280 μm
	# slits	8
	Min/Max slit width	10/40 μm
	Transmitting fraction of a'	54%
	Feature placement accuracy	0.5 μm
	Edge quality rms deviation	0.1 μm
	Pattern: S=slit, M=mask (μm)	
	20S-10M-20S-10M-40S-	
	30M-10S-10M-10S-10M-	
30S-40M-10S-20M-10S		
CA2	Si T	2.5 μm
	Au T	$0.62 \pm 0.05 \mu\text{m}$
	a	1000 μm
	a'	296 μm
	# slits	5
	Min/Max slit width	10/68 μm
	Transmitting fraction of a'	65%
	Feature placement accuracy	0.5 μm
	Edge quality rms deviation	0.1 μm
	Pattern: S=slit, M=mask (μm)	
	24S-10M-38S-42M-68S-	
	42M-38S-10M-24S	

then

$$Q(\sigma_b) \equiv Q_0 \left(\frac{\sigma_b}{\delta} \right)^2 \times \sum_{\text{pixels}} \frac{[\mathcal{P}_j(\sigma_b) - \mathcal{P}_j(\sigma_b + \delta) - \mathcal{D}(\sigma_b, \delta)]^2}{\mathcal{P}_j(\sigma_b) + \mathcal{P}_j(\sigma_b + \delta) + 2\mathcal{P}_0} \quad (16)$$

where δ is an arbitrary change in beam size (we use $\delta = 8 \mu\text{m}$), $\mathcal{D}(\sigma_b, \delta)$ is the difference between value of $\mathcal{P}_j(\sigma_b)$ averaged over all pixels (j) and the similarly averaged $\mathcal{P}_j(\sigma_b + \delta)$, \mathcal{P}_0 is an estimate of the effective electronic pedestal noise, and Q_0 is an overall normalization factor. The quantity \mathcal{P}_0 is inserted to prevent overweighting of differences between small pulse heights, and here is chosen to be the same as the peak value of $\mathcal{P}_j(\sigma_b)$ for a $50 \mu\text{m}$ pinhole at $E_b = 2.1 \text{ GeV}$. For optical elements that keep the primary image features well contained on the detector for modest beam sizes, $\mathcal{D}(\sigma_b, \delta)$ will be negligibly small; however, for very large beam sizes or optic designs with image features close to the detector edges, it can become significantly nonzero. The resolving power $Q(\sigma_b)$ is an approximate indicator of the

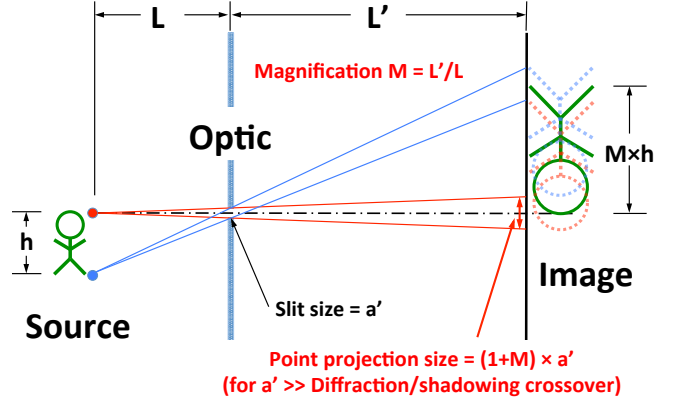


Figure 6: Simplified schematic of the basic principles of a pinhole camera.

inverse statistical error squared per unit beam current for a single bunch, single turn measurement at low beam current: Q_0 has been chosen so that the expected statistical uncertainty in beam size, $\Delta\sigma_b$, at the CESR-TA xBSM can be expressed as

$$\frac{\Delta\sigma_b}{\sigma_b} \approx \frac{10\%}{\sqrt{Q(\sigma_b) \times I(\text{mA})}}, \quad (17)$$

where I is the beam current. Note that for $Q(\sigma_b) = 1$ and the smallest beam current of interest, 0.1 mA, a barely acceptable measurement ($\sim 3\sigma$ separation from zero) is obtained at all beam sizes; *i.e.*, with this normalization, $Q(\sigma_b)$ values below unity indicate a region of beam size where resolving power is inadequate at the smallest beam currents. Our goal in optic design, then, is to obtain the broadest possible regions of beam size where $Q(\sigma_b)$ is not only larger than the alternatives, but also greater than unity. Not surprisingly, the biggest challenge is obtaining adequate sensitivity at small beam size, where small changes in relative beam size alter the image shape relatively less than at larger beam size.

Imaging of x-rays in the xBSM occurs according to the basic principles of a pinhole camera, which are shown in Fig. 6: ignoring diffraction, each point at the source projects to a band on the image plane that is the size of the pinhole scaled by $(1+M)$, where M is the magnification, whereas different points in the source plane separated by h project in an inverted manner to a separation of $M \times h$ at the image plane. As the pinhole gap size a' approaches the *diffraction crossover* (the aperture at which geometrical anti-shadowing recedes and diffraction dominates) from above, the image width will decrease because diffraction has a small effect relative to the anti-shadow of the slit. At the diffraction crossover, the image from a single slit is narrowest; below the diffraction crossover, the width of the image grows. However, the area of the image scales linearly with a' , regardless of the effect of diffraction on its shape; a consequence of these features is that the peak of the image lowers rapidly as a' shrinks below the diffraction crossover. These characteristics are evident in Fig. 7(a), which shows four point response functions for simple pinholes (slit sizes of 300, 100, 50, and 25 μm)

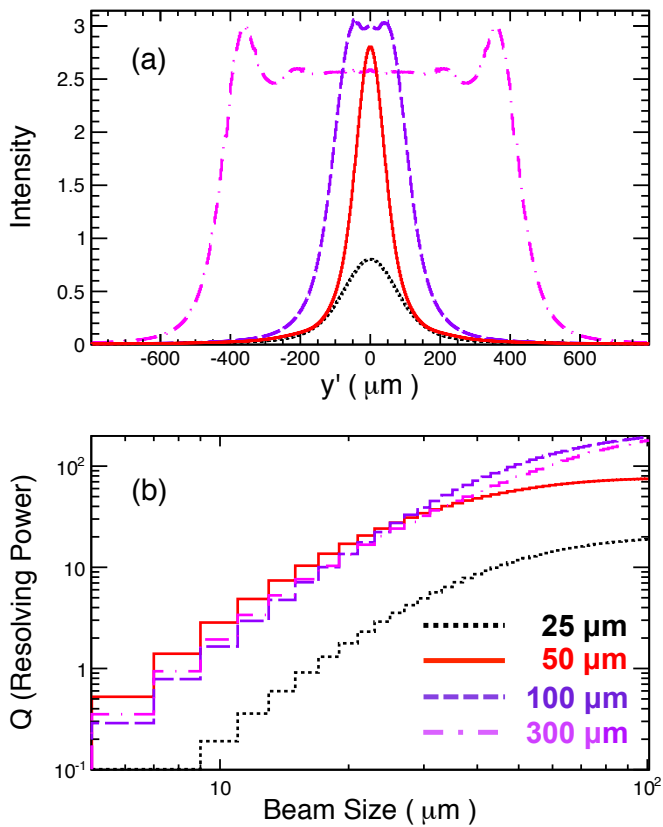


Figure 7: Predicted (a) point response functions and (b) beam-size resolving-power curves for pinholes of indicated openings, all at $E_b = 2.1$ GeV.

for $E_b = 2.1$ GeV and using a $4.4 \mu\text{m}$ diamond filter. In the absence of diffraction, all would be rectangular in shape, with widths at the image plane of $(1 + M)$ times the gap sizes (957, 319, 160, and $80 \mu\text{m}$, respectively). In this case the diffraction crossover is about $50 \mu\text{m}$.

The beam-size resolving power for four pinhole sizes is shown in Fig. 7(b), which highlights important principles applicable to optimizing effectiveness of optical elements: more light improves photoelectron-counting statistics, but for very small beam sizes, steep edges and/or narrower peaks in the prf outweigh greater total energy deposition. For example, better resolution is possible above beam sizes of $\sigma_b = 40 \mu\text{m}$ using a slit size of $300 \mu\text{m}$ compared to $50 \mu\text{m}$, because above that size neither has any steeply changing regions which offer high sensitivity, and the additional signal in the center of the distribution for the broader slit aids in distinguishing two nearby beam sizes. The crossover point for the $50 \mu\text{m}$ and $100 \mu\text{m}$ slits is even lower, at about $\sigma_b = 25 \mu\text{m}$. The optimal choice depends upon the beam size range of interest.

We have also explored the use of multi-slit optical elements, known as coded apertures. Coded aperture imaging is a technique well-developed among x-ray astronomers [39] which can, in principle, improve on the spatial resolution of a pinhole camera, due, in part, to much greater x-ray collection efficiency. A coded aperture has multiple slits, with the added feature that, depending on the fabrication technique, the mask material may

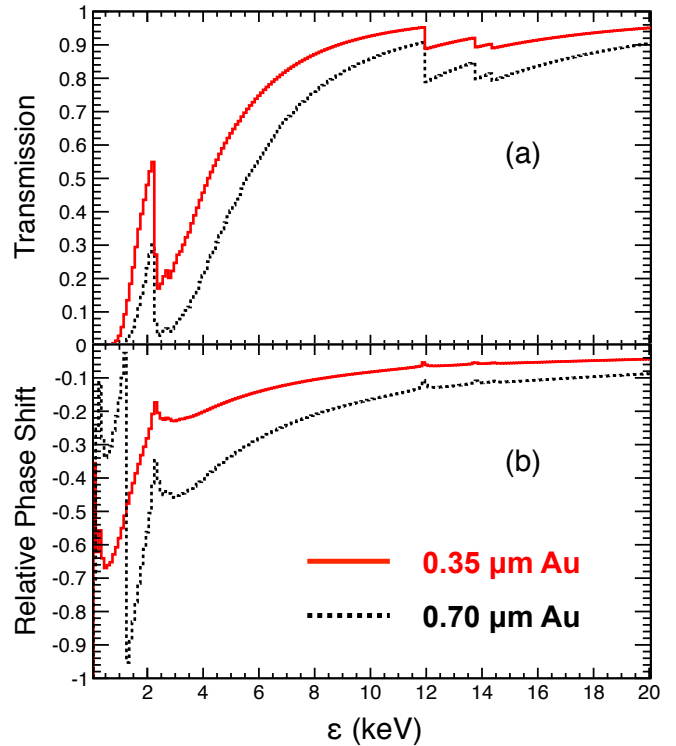


Figure 8: X-ray (a) transmission fractions, and (b) phase shifts (in units of 2π) as function of x-ray energy for gold masking of thickness $0.35 \mu\text{m}$ (dashed) and $0.70 \mu\text{m}$ (solid).

be thin enough to partially transmit x-rays with a phase shift. Through interference, light passing through the mask will affect the prf for good or ill, depending on slit and mask sizes and the x-ray spectrum. Our coded apertures use a gold masking material of 0.5 - $0.7 \mu\text{m}$ thickness on top of a $2.5 \mu\text{m}$ thick silicon substrate (which also absorbs some x-rays, but does so identically for both slit and mask regions). The effective transmission and phase shift of gold masking (with thicknesses 0.35 and $0.70 \mu\text{m}$) are shown in Fig. 8(a) and (b), respectively. In this example, the thinner masking is more effective than the thicker choice because it introduces a significant phase shift while preserving a larger fraction of the incident intensity for distribution among the peaks. To illustrate the effect of partially transmitting materials, Fig. 9 shows the prfs for several single slit optical elements of the same slit size ($50 \mu\text{m}$) but different masking thicknesses ($0.35 \mu\text{m}$, $0.70 \mu\text{m}$, and infinite). Note that the 0.35 -micron-thick gold has a large phase shift ($-\pi$ to $-\pi/2$) near the peak of the x-ray energy spectrum, in the 1 - 3 keV region. The finite-thickness masking introduces satellite diffraction peaks into the prfs through interference of phase-shifted x-rays with those that pass through slits. The corresponding resolving power of these three optical elements is shown in Fig. 9(b), where it is evident that the single-slit with thin-masking outperforms a single slit with thick masking below about $\sigma_b = 15 \mu\text{m}$.

Adding more slits can improve beam-size resolving power. Two identically-sized double-slit (50 - 20 - $50 \mu\text{m}$ slit-mask-slit

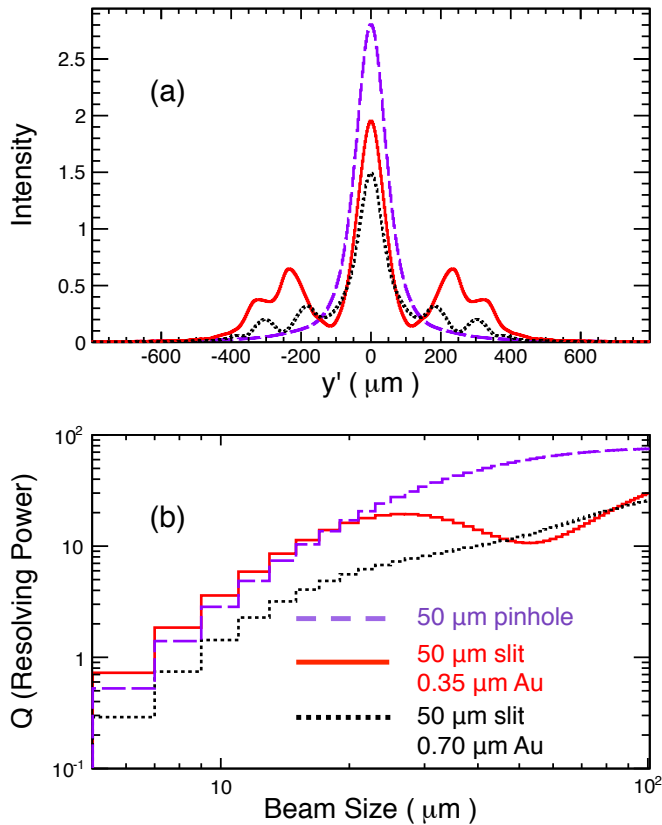


Figure 9: Predicted (a) point response functions, and (b) beam-size resolving-power curves for three different optical elements at $E_b = 2.1$ GeV, as indicated.

patterns) coded aperture prfs are shown in Fig. 10 for two thicknesses of gold masking. For the thinner masking material the valley between the primary peaks is deeper, the peaks themselves are higher, and the satellite peaks are more prominent. These features are seen to yield the expected effects in Fig. 10(b), where the resolving power comparisons reveal superior performance of the thinner masking (relative to thicker masking) below $\sigma_b = 45$ μm . Notice, however, that the single-slit 50 μm pinhole obtains better resolution (compared to the thin-mask double-slit CA) above about $\sigma_b = 25$ μm , and is better at all beam sizes below $\sigma_b = 100$ μm compared to the thick-mask coded aperture. Design of an optical element must account for slit pattern and mask effects as well as incident x-ray spectrum and target beam size; ignoring any of these details can result in a complex coded aperture that does not perform as well as a properly sized single slit with no masking material.

That the details of optical element design are subtle is exemplified by comparison of two slit designs that were fabricated for this application (Table 4) as well as two alternatives. Coded aperture CA1 is a Uniformly Redundant Array [40] with 31 elements and has been extensively evaluated in run periods to date; CA2 was designed with the conclusions of this section in mind, and will be used in our next run period. Comparisons are made at our smallest energy, as that is where performance is inhibited most by lack of light at low beam current. The prfs at $E_b = 1.8$ GeV are shown in Fig. 11(a) and (b), respectively;

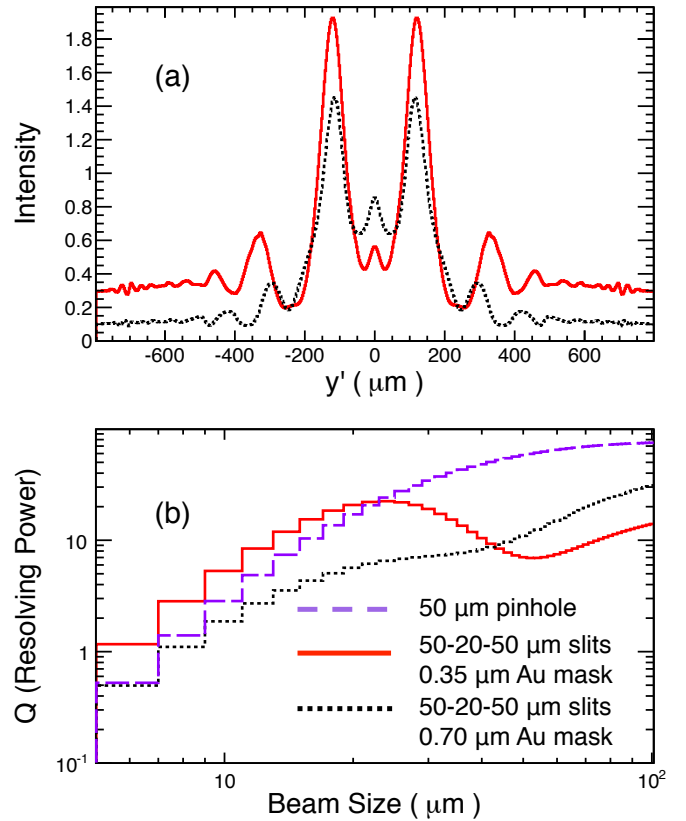


Figure 10: Predicted (a) point response functions, and (b) beam-size resolving-power curves for several optical elements at $E_b = 2.1$ GeV, as indicated. For comparison, (b) also shows the curve for a simple 50 μm pinhole, identical to that in Figs. 7(b) and 9(b).

beam-size resolving power is shown in Fig. 12. The key difference is wider and fewer slits in CA2 than for CA1; CA2 lets through more x-ray intensity, and has peaks with deeper and wider valleys. An even simpler design, denoted as 3S, features just three 60 μm slits separated from one another by 60 μm of masking; its properties appear in Figs. 11(c) and 12. Note that above $\sigma_b = 25$ μm , a simple 60 μm pinhole is superior in statistical resolving power of beam size, because above that size the valleys between the peaks in the coded apertures' prfs become populated, leaving the pinhole with steeper edges with which to provide resolution. CA1 has better resolving power than the pinhole below $\sigma_b = 9$ μm ; however, at this beam size, both have $Q(\sigma_b) \ll 1$. CA2 and 3S fare better than CA1 or the pinhole at moderate or small beam sizes. It is interesting to note that the slight superiority of CA2 over 3S at small beam size is reversed at $E_b = 2.1$ GeV, demonstrating the sensitivity of performance to optic design and x-ray spectrum.

3. Apparatus

Two installations of the xBSM are maintained at CESR-TA: one for electrons, and one for positrons. These are similar, differing only in the source-to-optic and optic-to-detector distances (L and L' , respectively, in Fig. 3), as shown in Table 3.

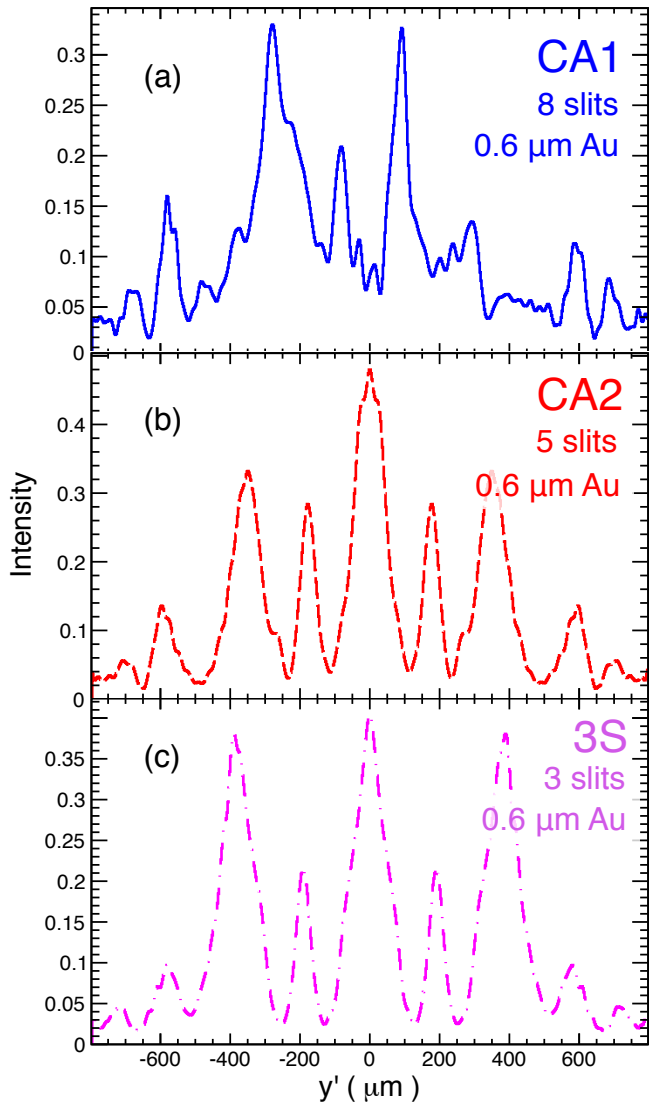


Figure 11: Predicted point response functions at $E_b = 1.8$ GeV, a $2.5 \mu\text{m}$ -thick Si substrate, and a $0.60 \mu\text{m}$ Au mask for (a) CA1 (8 slits: see Table 4), (b) CA2 (5 slits: see Table 4), and (c) 3S (3 slits: see text).

Each apparatus consists of four components: beamline, optical elements, detector elements, and readout. These are described below.

3.1. Beamline

During each of two annual CESR-TA run periods, two CHESS [41] (Cornell High Energy Synchrotron Source) beamlines and hutches are re-purposed for xBSM use. A windowless evacuated x-ray beamline, approximately 14 m in length, connects the detector box to the CESR vacuum, as shown in Fig. 13. There is no material impeding the x-ray beam except for purposely introduced optical elements, defining apertures, and filters, all described below. Thus, the detector box volume is in contact with the CESR vacuum. While the CESR vacuum is maintained at approximately 2×10^{-9} Torr, the detector box contains electronic components, printed circuit boards, ca-

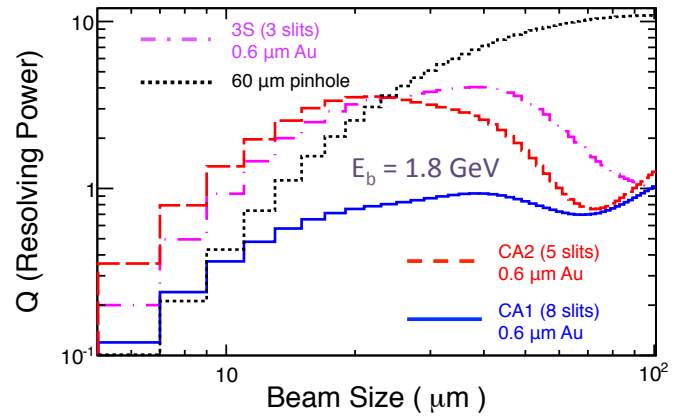


Figure 12: Predicted beam-size resolving-power curves at $E_b = 1.8$ GeV, for several optical elements (see Table 4 and text), as indicated.

bles, and cooling lines that are not vacuum compatible. The detector box vacuum is maintained at approximately 10^{-6} Torr. The differential pressure is maintained without contaminating the CESR vacuum by a series of apertures in the beamline that increase the impedance and by the use of turbo pumps in each section between the apertures. A fast gate valve, located 2 m upstream of the detector box, protects the CESR vacuum by closing if the pressure measured at the vacuum protection sensor (see Fig. 13) exceeds 10^{-4} Torr. This trip level corresponds to 10^{-6} Torr at the optic assembly due to the impedances and pumps. The windowless feature is essential for providing sufficient x-ray flux for single-shot capability at low beam energies and/or current (*i.e.*, having a viable beam size measurement from a single bunch on a single turn).

3.2. Detector

The detector is a linear array of InGaAs diodes with a $50 \mu\text{m}$ pitch and $400 \mu\text{m}$ horizontal width manufactured by Fermionics, Inc. [42]. Its parameters are summarized in Table 5. The active InGaAs layer is $3.5 \mu\text{m}$ thick and is covered by a Si_3N_4 passivation layer $0.16 \mu\text{m}$ thick. The time response of the detector is sub-nanosecond (see Sect. 3.4 below). The portion of a pixel sensitive to x-rays, which was measured by sweeping a narrow vertically limiting aperture immediately upstream of the detector, is slightly smaller than the full pitch. Hence there is no overlap in the response of adjacent pixels, which would otherwise alter the effective prf; neither is there an appreciable insensitive region of more than a few microns between adjacent pixels. While this detector is marketed for detection of ultraviolet radiation (150 nm), we have found that it performs well in the x-ray (1 nm) range. A measurement of the detector spectral response is detailed in Sect. 5.1. Other commercially available detector arrays tested did not meet the sub-ns time response requirement.

The detector, shown in Fig. 14, is attached to a custom-designed printed circuit board. The common cathode of the detector array contacts the center trace through conducting epoxy.

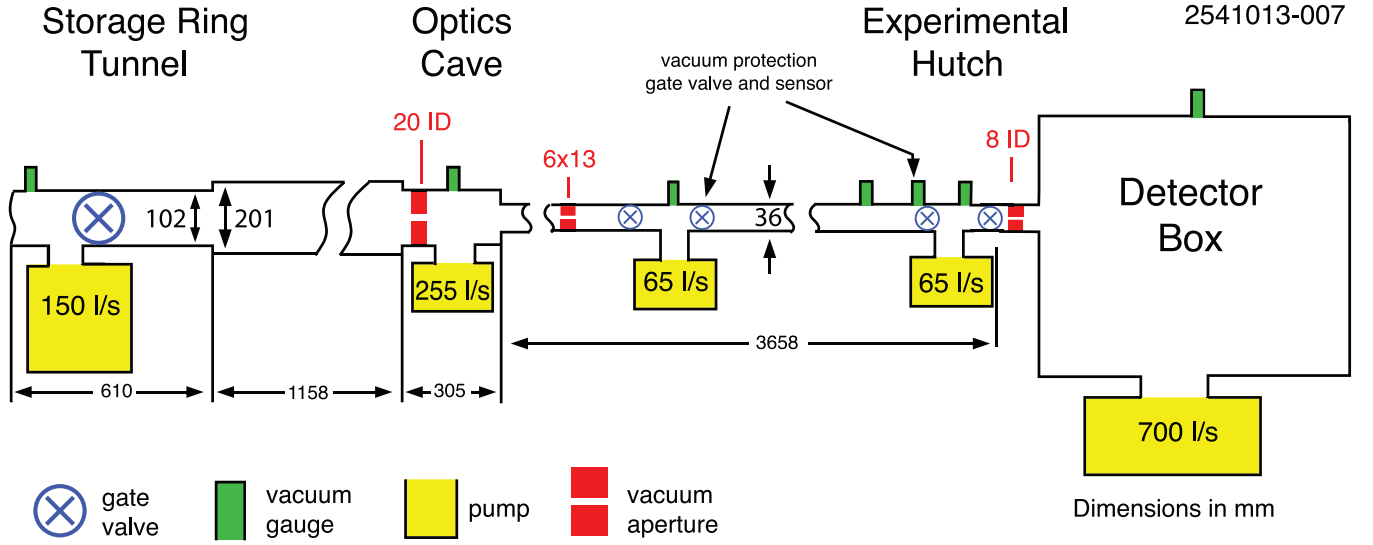


Figure 13: Layout of a CESR-TA xBSM beamline showing locations of pumps, impedance apertures, vacuum gauges, and relevant dimensions, in mm.

Table 5: CESR-TA photodiode array characteristics. All quantities marked (*spec*) are as specified by the manufacturer. The active pixel width was measured in our apparatus.

Parameter	Value
# channels, contiguous working (<i>spec</i>)	64
# channels read out for beam-size images	32
Pitch (<i>spec</i>)	50 μm
Active pixel height (<i>measured</i>)	45 \pm 3 μm
Horizontal width (<i>spec</i>)	400 μm
InGaAs thickness (<i>spec</i>)	3.5 μm
InGaAs density	5.5 g/cm ³
Si ₃ N ₄ thickness (<i>spec</i>)	0.16 μm
Si ₃ N ₄ density	3.25 g/cm ³

Contacts of contiguous anodes alternate between the left and right sides of the array. The printed pattern allows fabrication

Table 6: CESR-TA attenuator and filter characteristics. The attenuation of any limiting aperture alone is approximately the width relative to the active detector width of 400 μm .

Material	Thickness	Horizontal aperture
None	-	1 – 2 mm
None	-	171 μm
None	-	105 μm
None	-	35 μm
Diamond	4.4 \pm 0.1 μm	105 μm
Diamond	4.4 \pm 0.1 μm	50 μm
Diamond	4.4 \pm 0.1 μm	1 – 2 mm
Molybdenum	1.91 \pm 0.06 μm	1 – 2 mm
Aluminum	7.2 \pm 0.7 μm	1 – 2 mm

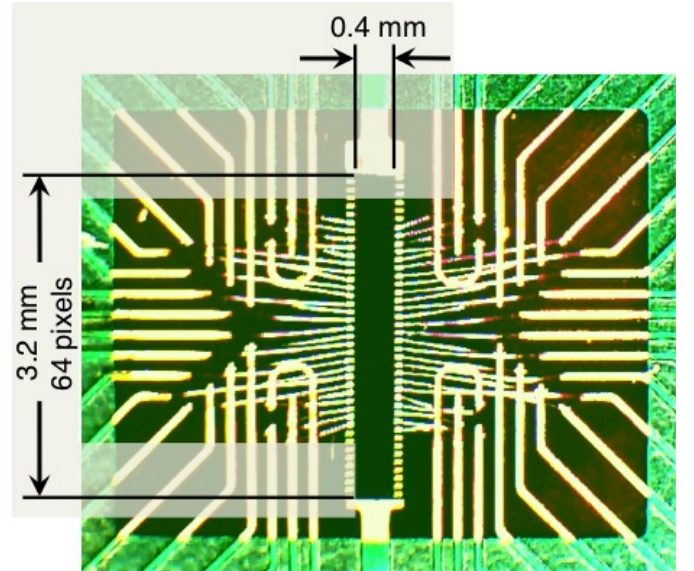


Figure 14: Annotated photograph of the CESR-TA xBSM photodiode array on its mounting board.

with 0.25 mm center-to-center trace technology, and limits the bond length to 2.2 mm.

The central 32 contiguous diodes of the array are used to measure single-shot vertical profiles. Eight additional channels are connected for diagnostic single-diode readout mode (Sect. 4.2). Another 3 diode elements are attached to each of 4 ground lines to reduce noise in the single-diode readout. Thus, there are 45 connections to the printed circuits mounting board: 32 contiguous elements, the 8 single diode readout elements, 4 grounds, and the common cathode.

The detector board is mounted on a preamp board, which, in turn, is attached to a stage with motor controlled horizontal and vertical motion, as shown in Fig. 15. This stage provides mo-

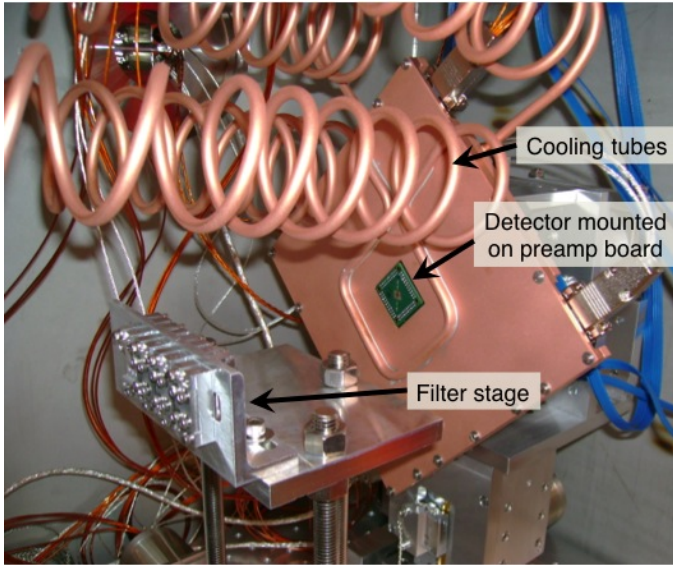


Figure 15: Annotated photograph of the CESR-TA xBSM detector mounted on its preamp board and movable stage, inside the vacuum of the detector box. A water cooled copper jacket surrounds the preamp board. Cooling tubes and the filter stage area also visible.

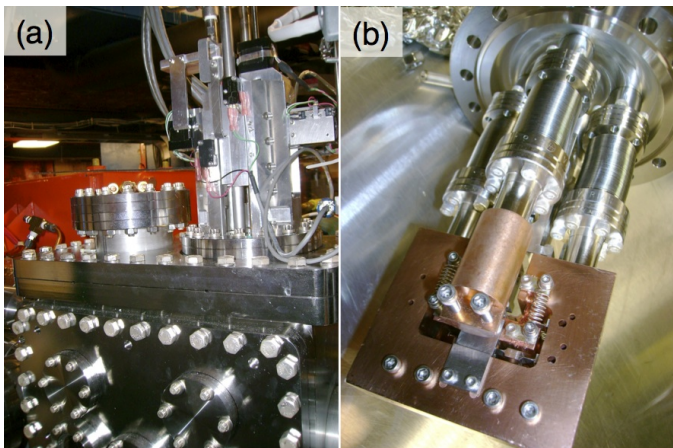


Figure 16: (a) The xBSM optics assembly mounted in the beamline. (b) Motors visible on the top control the vertical locations of two optics stages and the pinhole gap size.

tion necessary for alignment (Sect. 4.2). Also visible in Fig. 15, a set of filters and horizontally limiting apertures (attenuators) are mounted inside the detector box 75 mm upstream of the detector itself. Their properties are summarized in Table 6. The filters were selected to alter the x-ray spectrum incident on the detector in order to probe sensitivity of the detector and beam size measurement to wavelength. The attenuators are used to protect the detector and prevent preamplifier saturation by limiting x-ray flux in high current and/or high electron beam energy operation.

3.3. Optical elements

Optical elements are located in a dedicated enclosure in the beamline, shown in Fig. 16(a), approximately 10 m upstream of the detector box and 4 m downstream of the source point.

They are mounted on a stage, shown in Fig. 16(b). The three struts provide vertical motion and water cooling. Optical elements which have been tested include a pinhole, coded apertures of different designs, and a two-dimensional Fresnel zone plate. Each of these can be separately inserted into the beam with motor controls.

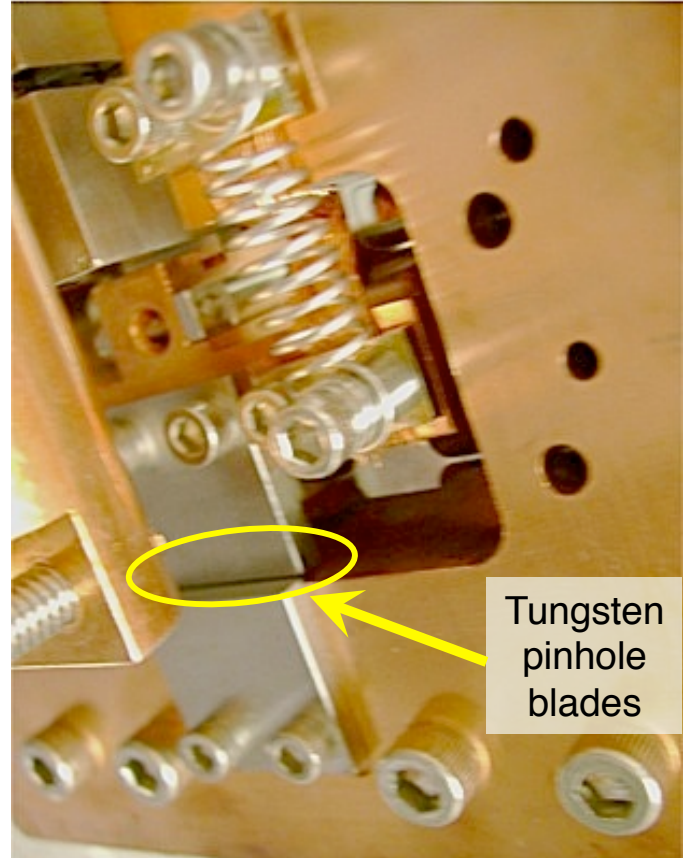


Figure 17: Annotated photograph of the tungsten blades forming the pinhole for the CESR-TA xBSM.

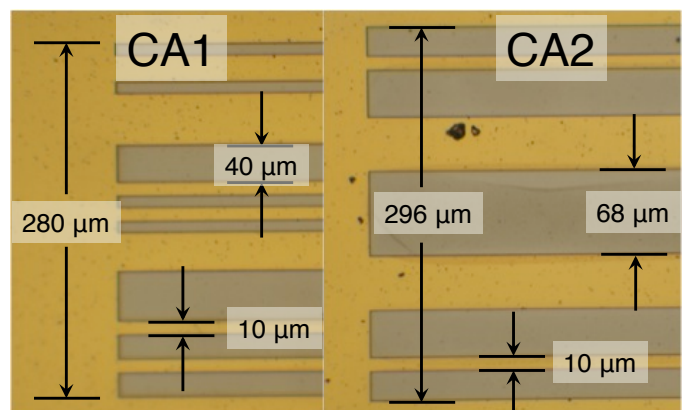


Figure 18: Photographs of portions of CESR-TA xBSM coded aperture optical elements CA1 (left) and CA2 (right). Dark strips indicate transmission slits, while lighter areas represent the gold coating. The imperfections (black spots) are remnants of etching resist with thickness $\sim 0.01 \mu\text{m}$, which are essentially transparent to x-rays.

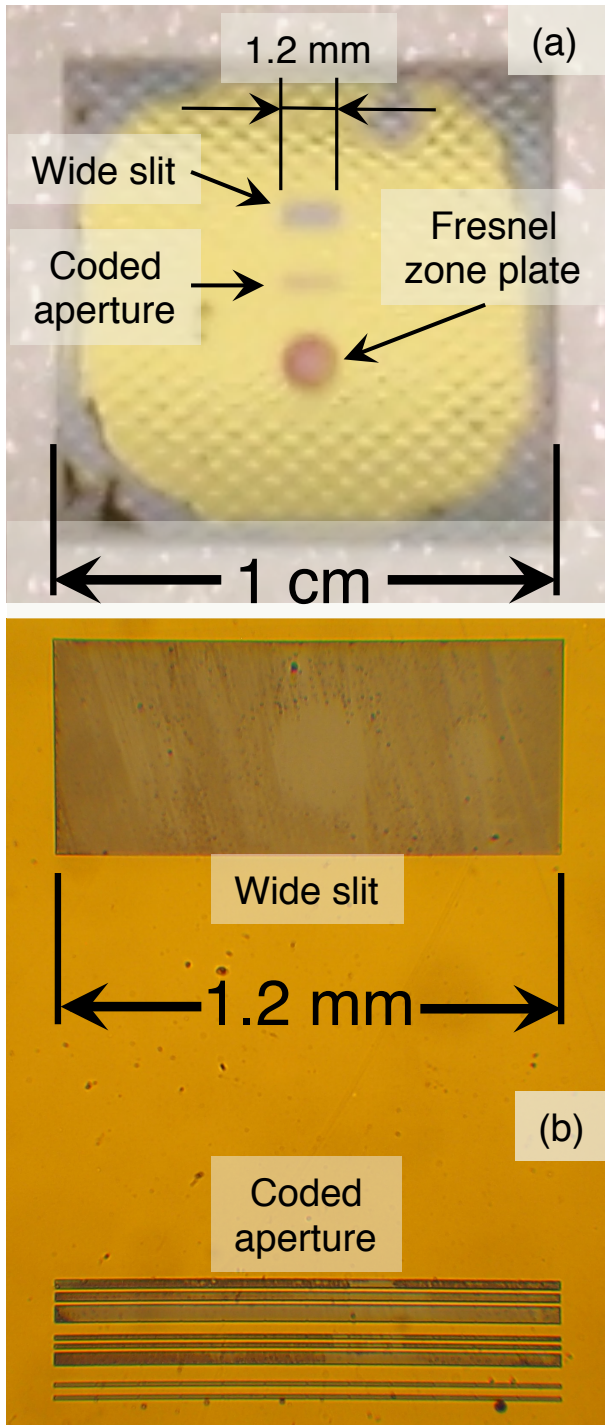


Figure 19: Annotated photographs of the silicon substrate optics chip. (a) Three optical elements are (barely) visible in the center of the 1-cm-square chip. (b) The coded aperture and simple rectangular hole are visible with reflected light. For scale, the common width of the features is 1.2 mm.

The one-dimensional pinhole is the simplest optic: a vertically limiting slit. The adjustable slit consists of two tungsten blades, each 2.5 mm thick, as shown in Fig. 17. The vertical location of the upper blade is motor-controlled through one of the struts: its position sets the slit opening. A 0.25 mm offset of the two blades along the beamline allows the opening to be completely blocked without any contact between the blades. Faces

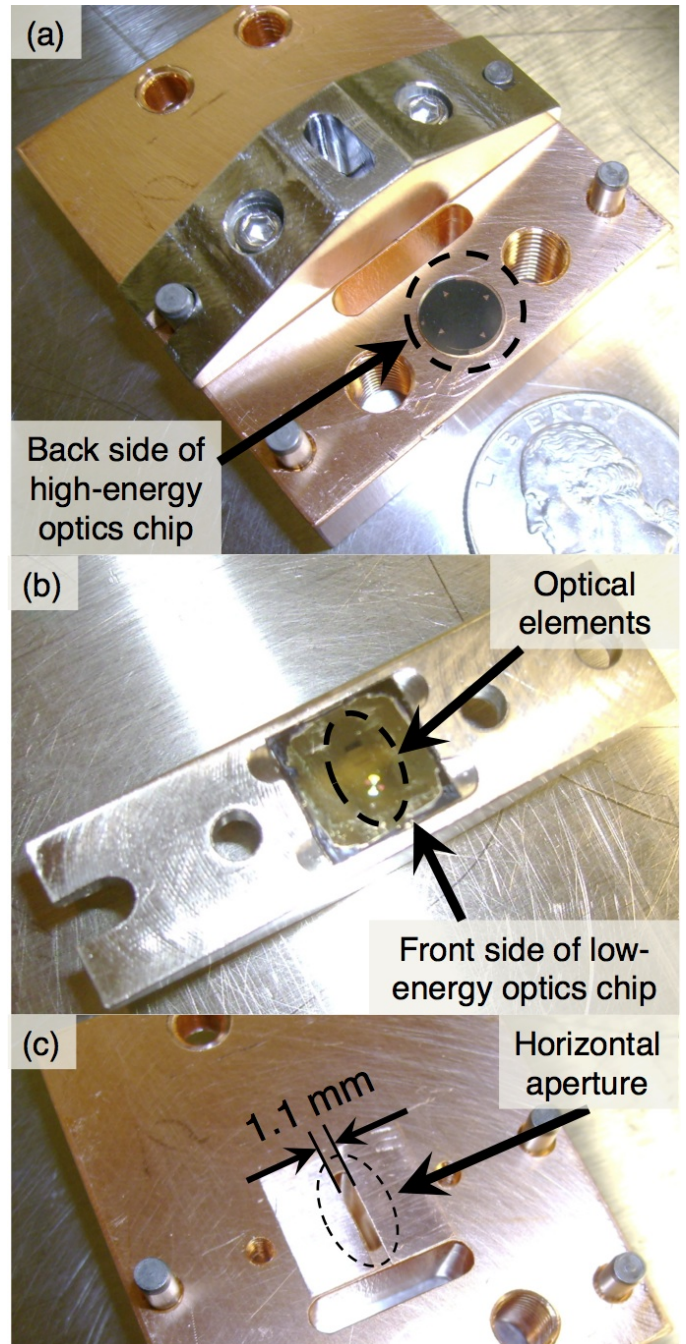


Figure 20: (a) The copper support block that attaches to one of the struts in Fig. 16(b) holds 2 optics chips. Here, one chip is exposed while the other is behind the stainless steel cover. (b) An optics chip is shown mounted in the stainless steel cover. (c) For low energy chips, the copper mounting block provides a 1.1 mm horizontally defining aperture.

of the tungsten blades forming the slit are tapered away from the incident x-ray beam by an angle of 2° to prevent small angle reflections off the faces from reaching the detector. For the x-ray spectrum at typical operating beam energies, 1.8-2.6 GeV, the gap size that results in the narrowest central peak in the image is in the range of 45-60 μm ; travel of the upper blade allows openings from zero up to 200 μm . A 500 μm -wide horizontal collimator sits just upstream of the pinhole to preclude x-rays reaching the detector via any path not passing through the pinhole and to limit the depth of field (*i.e.*, the longitudinal spread of the source).

A coded aperture, a 500 μm -wide slit, and a Fresnel zone plate are available. These were acquired from Applied Nanotools, Inc. [43], and are etched with a proprietary process into a thin gold layer on a 2.5 μm -thick silicon substrate chip. The two coded aperture designs we are using for low energy running, CA1 and CA2, appear in high resolution photographs in Fig. 18, and have parameters summarized in Table 4. Optical measurements indicate that the systematic placement of features is within 0.5 μm of the specifications. Edge quality of the etching is better than 0.1 μm rms deviation. The full optics chip which contains CA1 is shown in Fig. 19(a), and a view of the entire CA1 and wide slit in Fig. 19(b).

Optics chips are mounted on a copper support block which provides precision alignment and thermal contact, as shown in Fig. 20. A 1.1 mm horizontally limiting aperture in the support block stops x-rays that are transmitted through the gold outside of the etched pattern. A stainless steel cover plate, shown in Fig. 20, presses the optics chip into the copper, enabling precision alignment. The support block is, in turn, mounted on a separate vertical stage downstream of the pinhole (foreground of Fig. 16(b)).

Coded apertures suitable for higher energy running have been tested at beam energies of 4 GeV and above. The mounting block shown in Fig. 20(a) shows one of these devices: a round 350 μm CVD (synthetic) diamond substrate with a pattern (not visible) etched into 8.7 μm -thick gold masking. This device is discussed elsewhere [44, 45].

Performance of the pinhole and coded aperture are described in Sect. 5. The Fresnel zone plate was included in early optics chips as an option. This Fresnel zone plate is designed to focus 2.5 keV x-rays in two dimensions. When used with a wide spectrum x-ray beam and a one-dimensional detector, however, beam size resolving power is low. Use of an x-ray monochromator can address the wide spectrum, but only by limiting the number of photons to about 1% of those generated in the bend magnet, and so does not improve the resolving power enough for use in single-shot operation.

3.4. Readout & data acquisition

The xBSM electronic readout system has three main functions: (i) to amplify each pixel's photodiode signal, corresponding to $1-10^4$ photoelectrons, synchronously with bunches passing the source point separated by as little as 4 ns; (ii) to digitize the resulting voltage; and (iii) assemble the digitized data for all channels from each turn and bunch into a data file. This challenge is met with a system designed fully in-house. Each of 32

independent readout channels consists of a transimpedance amplifier, a variable gain amplifier, an analog to digital converter, a field-programmable gate array (FPGA), a local buffer, and a programmable sample clock delay.

Hardware components are modular, and are positioned both inside and outside the evacuated detector box in custom housings. Figure 21 shows an overview of this system. Components inside the detector box are represented in major block on the left. Signals from the diode detector are received, amplified and converted to differential signals prior to being delivered out of the detector box in bundles of 8 channels of twin-axial cable. Components outside the detector box are represented in the major block on the right. The bundle of 8 differential signals is received by a carrier board (represented as a separate sub-block) that handles 8 channels of signal conditioning and digitization.

Figure 22 shows the functional blocks of each channel's signal processing. After a 500 MHz low-pass filter, each channel provides 12 dB of fixed gain and -4 dB to 20 dB of digitally controllable gain in 24 steps of equal size. In "automatic gain control" mode, the readout software tests the signal and then

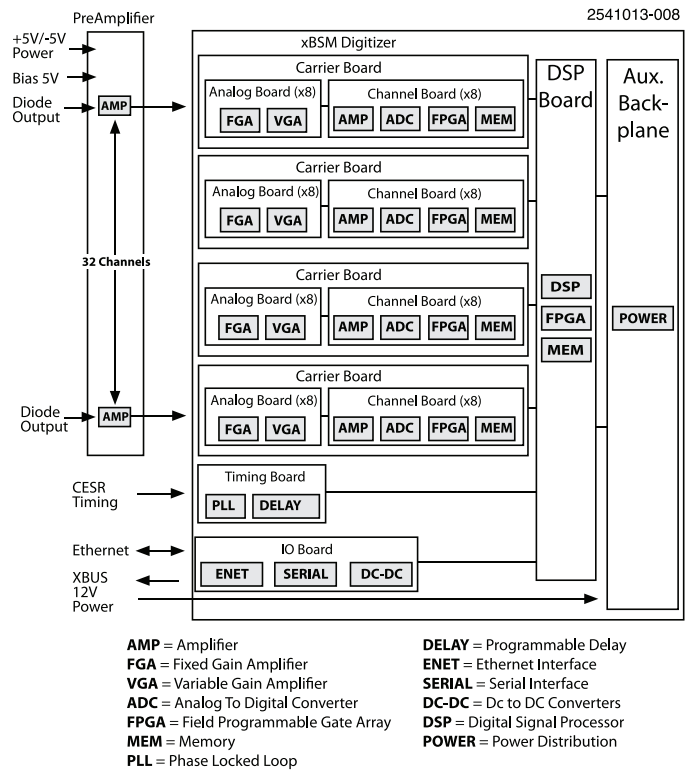


Figure 21: The CESR-TA xBSM electronics design.

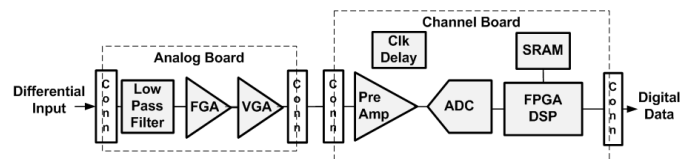


Figure 22: The CESR-TA xBSM function diagram of a single readout channel.

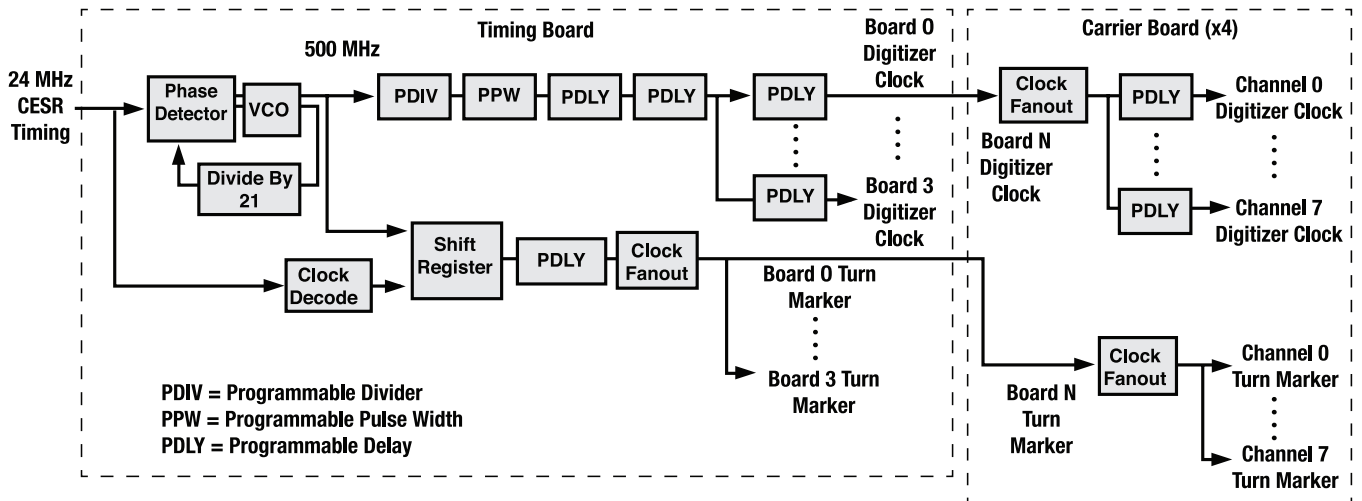


Figure 23: The CESR-TA xBSM signal chain timing.

sets the gain of all channels to the same, single highest value that does not saturate any single channel.

A 10-bit analog-to-digital converter sampling at 300 MHz is utilized to provide the requisite timing performance. The data from the converter is streamed through a local FPGA and is stored locally for each channel in an 18 Mbit SRAM. This allows for 10^6 samples to be captured on each channel without data compression. Each channel receives its own sampling clock signal and has an in-channel configurable delay to allow for channel-to-channel synchronization.

Synchronization to the CESR timing system occurs via a 24 MHz encoded data signal. This signal, synchronized to the CESR RF system, also contains revolution (turn) markers with a frequency of 0.4 MHz and acquisition triggers. The same timing signal is also delivered to all of the storage ring beam position monitors, so that synchronized turn-by-turn measurements can be shared by both systems.

A more detailed description of the internal timing control and distribution is provided in Fig. 23. An on-board voltage controlled oscillator generates a 500 MHz source clock synchronized to the 24 MHz encoded signal. This clock drives a divider with a programmable pulse width in order to provide a fully configurable sampling clock. The sampling clock signal passes through a series of common programmable delays prior to being fanned out to each of the four carrier boards. There are separate programmable delays at the carrier board level. The clock signal on the carrier board is then fanned out to the 8 sampling channels. Every channel has its own programmable delay, allowing precise adjustment of the sample point. The timing board also extracts the turn marker from the 24 MHz encoded signal. The turn marker passes through its own set of programmable delays and is fanned out to the 4 carrier boards where it is delivered to the individual channels. Each channel can then be synchronized to the accelerator revolution frequency. The digitizers run continuously. A bunch pattern describing the time structure of filled RF buckets in CESR serves

as a gating signal provided to all channels for determining when the sample is to be stored in the local SRAM.

During CESR-TA calibration procedures, 4-ns-spaced bunches can be measured in detail. The digitizers can be operated in waveform-capture mode by shifting the sample time of subsequent measurements. Figure 24 shows the resulting digitized signal of two 4-ns-spaced bunches of electrons. The waveform-capture mode is used for the timing calibration, discussed further in Sect. 4.4, in which the programmable delay for each channel is adjusted in 10 ps increments to center the sample point on the peak signal time. Drift in these settings is small compared to the width of the optimal sampling section of the peak of the diode waveform. The main source of drift in the delay chips is thermal loading, but as the data acquisition hardware is temperature-regulated, any remaining effect is small over the period of a day. The delays are tuned prior to each experimental shift. Variation in the RF phase due to beam loading has an effectively negligible effect on the accuracy of the sampling point.

The digital data from each channel is collected on the digital signal processing (DSP) board. This board allows for on-instrument processing and data manipulation. It also provides the link to the ethernet interface which is contained on the board. All controls and data flow are transmitted via an ethernet interface. A diagnostic interface is provided via a serial fieldbus (XBUS) connection on the IO board. Power is delivered to the various boards via the auxiliary backplane.

Finally, digitized pulse heights are assembled into a text raw data file which constitutes a *run*. Each file begins with a number of lines specifying characteristics of the run, including its sequential number, a date and time stamp, whether it contains electron or positron data, motor control settings on optic, filter, and detector elements, beam energy, beam current, bunch pattern, digital gain range setting, and pedestal and gain values for the 32 channels of readout. These are followed by a sequence of ordered lists, each of 32 numbers corresponding to the 32

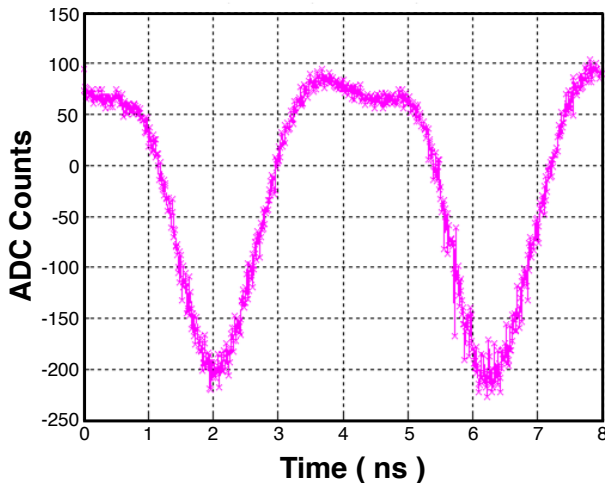


Figure 24: Pulse shape vs. time of the CESR-TA xBSM photodiode readout.

contiguous pixel adc values. Single bunch runs generally span from 100 to 64×10^3 turns, with 1024 turns most common. Multi-bunch runs typically also contain 1024 turns per bunch for up to ~ 50 bunches; the number of turns is limited by the size of the SRAM as $\sim 10^6/(\# \text{ bunches})$. For multi-bunch running the data file has turn-by-turn data for bunch #1, followed by turn-by-turn data for bunch #2, and so forth. Data files are maintained on a backed-up RAID array for subsequent offline analysis.

4. Operations

Each CESR-TA run period typically has a duration of 9-21 days. Hence physical installation, data acquisition checkout, alignments of the detector and optical elements, and setting of the pinhole size are necessary for each such run period. Alignment and calibrations can change slightly during each run period, requiring re-tuning and re-calibration from day to day, and the pinhole optic is set to have a different gap size for each beam energy.

4.1. Installation

Prior to each CESR-TA experimental run period, the xBSM hardware is installed into the CHESS hutches, one that is illuminated by x-rays from the positron beam and the other by x-rays from the electron beam. The hardware is broken into two main assemblies, the vacuum controls and the detector box. Each assembly is mounted on a rolling frame and is placed into storage during CHESS user experimental run periods. The hardware is rolled into the hutch, placed on rigid stands, and bolted to the vacuum chamber bringing the x-ray beam to the hutch. The basic installation process places the hardware roughly into the same position it was in at the conclusion of the previous CESR-TA run period. Both assemblies have survey monuments permanently mounted on critical components (flanges, box corners, beam pipes). These monuments are used in conjunction with survey monuments within

the hutch to locate the hardware to within 0.5 mm of the previously known good location, which had been empirically determined to produce proper beam size measurements. The xBSM alignment process is described further in Sect. 4.2.

After the hardware has been properly installed and positioned, the vacuum controls are used to initiate the pump-down of the detector box. A differential pumping scheme is utilized which requires the detector box to be brought down to 10^{-5} Torr before the upstream gate valves are opened to allow the transmission of x-rays from the source. The initial pump-down takes approximately six hours due to an accumulation of contaminants during storage. Once the pressures have stabilized and the gate valves are open, the system becomes ready for subsequent pre-operational alignment and calibration.

4.2. Detector & Optic Alignment

Initially the detector box and optical elements are positioned via an optical survey to an accuracy of 0.5 mm (Sect. 4.1). However, the θ -dependence of the x-ray spectrum and intensity (Eqs. (3), (4), and (6), as well as Table 2) introduces sensitivity to variations in the e^\pm orbit that typically occur in the storage ring during day-to-day tuning. The alignment procedure also provides an initial check on the general beam quality. Prior to alignment, the storage ring orbit is set to a nominal working point and a low-emittance-tuning procedure is used to minimize vertical beam size. The detector is reset to a standard working position for the pinhole optic in both the vertical and horizontal directions. During the alignment, minor corrections are made to both the electron orbit and the positions of the detector and optical elements.

The alignment procedure starts with scans wherein the detector position is slowly moved through its horizontal and vertical degrees of freedom while its position and synchronized response are periodically recorded. As described in Sect. 3, the detector is mounted on a stepping-motor controlled stage which allows vertical and horizontal motions of ± 10 mm. Completion time for each scan is ~ 1 minute. The current from a single diode in the array is monitored, with readings in the $0.1 \mu\text{A}$ range; the diode is biased with the cathode at ground and the anode connected to an ammeter input. Several such diodes are available, located just outside the array of 32 contiguous diodes connected to the digital readout, as shown in Fig. 14. Typically, we use a diode that is 0.925 mm from the center of that array. The diode array position in the vertical direction is adjusted in order to center the single diode on the nominal detector position.

In the first step of the alignment procedure, the detector is brought to a vertical reference location known to be in the nominal plane of the storage ring. This is a preliminary position and may change with subsequent tuning of the storage ring (see below). Steering corrector magnets are used to move the horizontal e^\pm orbit in the storage ring to a reference orbit that is known to project light down the CHESS beam line. The vertical orbit is corrected to be flat (*i.e.*, in the plane of the storage ring) at the source point for the x-ray beam line. The detector, read out in single-diode mode, is then exposed to the x-ray beam with no optical element in place.

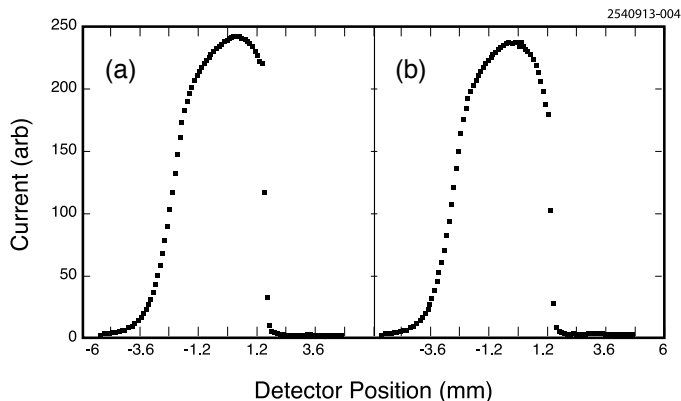


Figure 25: Single-diode current draw (arbitrary units) vs. vertical position of the detector stage as it is moved through an x-ray beam from 2.6 GeV electrons with no optical element in place, both (a) before, and (b) after adjustment of the electron beam orbit. The vertical width of the x-ray beam observed here is $\sigma \approx 1.1$ mm. The distribution in (a) is clipped above a position of 1.3 mm by the edge of an element in the beam line, whereas in (b), the electron orbit has been adjusted to move the x-ray beam slightly away from the obstruction.

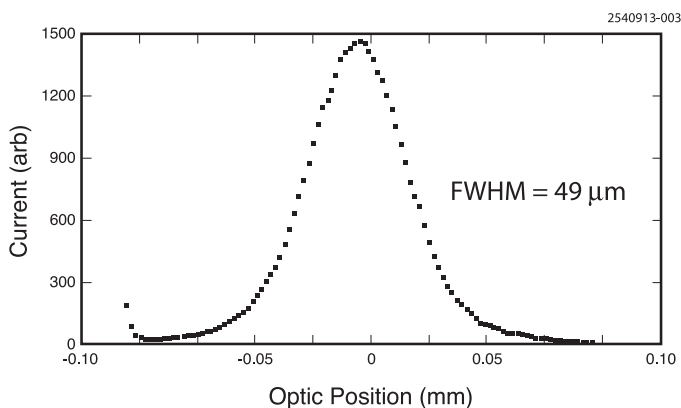


Figure 26: Single-diode current draw (arbitrary units) vs. vertical position of the optical element stage, using the pinhole optic with an opening of ~ 40 μm . These data were taken just after the orbit adjustment shown in Fig. 25.

Typical initial vertical beam profiles are shown in Fig. 25, which feature widths consistent with that predicted by Eq. (6) and shown in Table 2. This example of an initial vertical beam profile has a single-diode current distribution that is truncated near one extreme of its vertical range, indicating that the x-ray beam has been missteered into an aperture. This condition is corrected by fine-tuning the stored beam orbit.

The significant clipping visible in Fig. 25(a) was reduced to that shown in Fig. 25(b) with a subsequent orbit adjustment which moved the center of the x-ray profile to a lower position, away from the aperture limitation. The goal with such adjustments is to move the vertical position and direction of the x-ray beam such that the detector can be centered on the beam envelope and any aperture clipping is beyond the edge of the detector. In this example, the preliminary working position of the detector center is -0.26 mm on the scale shown, while the center of the x-ray beam envelope is at -0.16 mm. A small correction to the detector position is made to center it on the beam. While the clipping still exists after the orbit adjustment

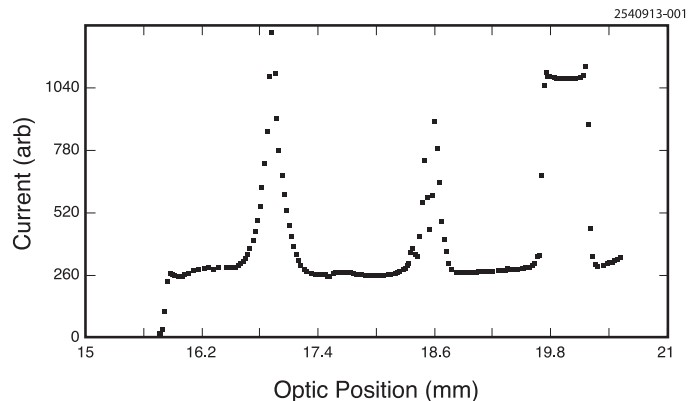


Figure 27: Single-diode current draw (arbitrary units) vs. vertical position of the optical element stage. These data were taken just after the scans of Figs. 25 and 26. Over this range, three elements of a gold-masked silicon optics chip are illuminated: a Fresnel zone plate is centered at ~ 16.9 mm, a coded aperture at ~ 18.5 mm, and a 0.5 mm-wide single slit at ~ 20.0 mm. The non-zero intensity between the elements is a measure of transmission through the gold masking.

in this example, the beam profile is unaffected up to 1.3 mm from the peak, which is more than the 0.8 mm half-width of the detector. After this step, the e^\pm beam orbit and detector vertical position (accounting for the offset between the single diode and the center of the detector array) are fixed for subsequent data acquisition. At this point, a horizontal scan of the detector in single-diode-readout mode is performed to ensure that there is no upstream aperture limitation near the operating position; any clipping observed within the horizontal detector span indicates a severe distortion relative to the reference orbit. After the root cause of any such distortion is found and addressed, the alignment procedure must be restarted.

In the next step, the optical elements are centered on the line between the x-ray source point and the detector. The pinhole optic is mounted on a stage that allows vertical motion. Fig. 26 shows the result of scanning the pinhole optic through the beam while logging the current in the single diode. The location of the peak, in this case, -0.005 mm, is used to locate the pinhole in subsequent data runs. The pinhole optic has a 0.5 mm horizontal aperture. The detector horizontal position is adjusted to center the detector on the line defined by the x-ray source and the optic aperture by conducting a single-diode scan of the detector in the horizontal direction.

The pinhole alignment provides a first measurement of the beam quality. The observed width of the distribution in Fig. 26, taken at the plane of the optical element, is proportional to that of the convolution of the prf with the magnified beam size, traced back from the detector plane to that of the PH optic. For Fig. 26, where $\text{fwhm} \approx 49$ μm in the plane of the optic, this convolved rms width, referred to the source plane, is $\approx (1 + 1/M) \times \text{fwhm}/2.36$, or ≈ 30 μm . This is a common operating condition for CESR-TA at $E_b = 2.1$ GeV. Had this rms value been much larger, it would have indicated that either the emittance or vertical beam motion were unacceptably large. Such conditions would require retuning the orbit and repeating this alignment procedure.

To align the etched-gold optical elements, the pinhole stage

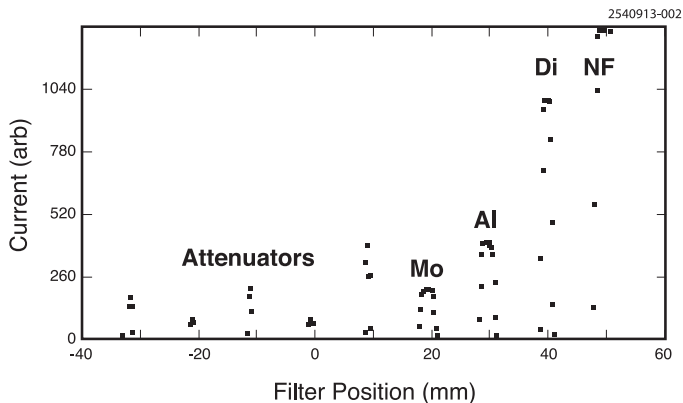


Figure 28: Single-diode current draw (arbitrary units) vs. vertical position of the filter stage, just upstream of the detector. These data were taken just after the scans of Figs. 25, 26, and 27. The locations of several filters and attenuators are indicated.

is retracted and the optics chip moved into position. Figure 27 shows the result of a single-diode scan of the optics chip through the beam. The location of the center of the coded aperture, in this case 18.5 mm, is used to locate the coded aperture in subsequent data runs. As described in Sect. 3, these optical elements have a horizontal aperture of 1.1 mm. As this aperture is not aligned to the pinhole horizontal aperture, a separate horizontal detector alignment is required. The horizontal position of the detector is adjusted by conducting a single diode scan while varying the horizontal location of the detector box. The detector box horizontal position is adjusted, rather than the horizontal position of the detector within the box, to preserve the alignment of the filter elements (described below) with respect to the detector.

Filter elements, used in the x-ray spectrum analysis described in Sect. 5.1, are located on a motor-drive stage in front of the detector, as shown in Fig. 15. A single-diode scan of the filter element stage is performed to locate the operating positions of the filters. Figure 28 shows the stage location for various filters and horizontally limiting apertures.

Final alignment is accomplished using the digital detector readout of the full 32 channels by adjusting the vertical detector location to center the diode array on the x-ray beam. To center the detector on the x-ray beam envelope and to center the image on the detector, minor adjustments, on the order of 100 μm , can be made to the detector and optic vertical positions and/or the beam orbit.

4.3. Beam-induced coded aperture damage

The sub-micron gold masking on coded apertures can be damaged by exposure to power above a certain level. Care must be taken to limit flux by use of attenuators (horizontally limiting apertures) and adequate heat sinks for the gold masking. In one instance where adequate precautions were not taken, such damage did occur to one CA1 element. It was noticed that image patterns changed, and later the optic was removed from service. A photograph appears in Fig. 29, and shows evidence of alteration of the masking by overexposure to the beam. Image data

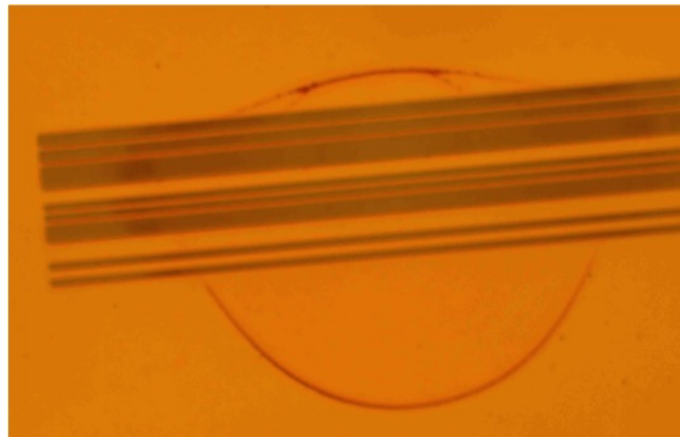


Figure 29: Photograph of a CA1 optical element after accompanying data showed an alteration in image shape. Excessive x-ray power on the optic has damaged the gold masking.

taken before and after the damage occurred indicate that a significant fraction of gold masking was removed from the chip in the central, etched region of the pattern; the darkened arcs in the photograph, taken with reflected light, may or may not correspond to such regions. The damage may be due to raising the temperature of the optics chip above the silicon-gold eutectic point, 363°C. It is estimated that the beam exposure causing this damage was ~ 22 mW. The damaged CA1 element had thinner gold masking (0.53 μm) than any other optic chips we have used; thicker gold improves heat transfer to the mounting (Fig. 20), enabling higher operating power without damage.

4.4. Calibrations

After the instrument has been properly aligned and the detector and optics are deemed to be in a healthy state, the data acquisition system is brought online and configured. The xBSM requires tight synchronization with the storage ring master timing controls in order to take bunch-by-bunch and turn-by-turn measurements. Timing controls within the data acquisition box are used to separately align each of the 32 channels to a reference bunch (train 1, bunch 1) in the storage ring. Typically, the time domain synchronization can be accomplished with an accuracy of ~ 50 ps. Once this synchronization is established, all timing control settings are saved to disk, making the instrument ready to capture detector images of individual bunches in the storage ring.

Digitized readout of each pixel's pulse height on a particular bunch and turn requires four different types of electronic calibration corrections: pedestal, gain, preamplifier range, and bunch-to-bunch crosstalk. Under normal conditions, all channels are set in common to one of the 25 ranges for each run. Each range provides ± 512 counts of readout; the ranges cover a dynamic range of ~ 15 , in logarithmic steps (nominal 1 dB per step). Pedestals, typically a few counts, apply to each channel in each range, although they tend not to vary with range. Gains provide a multiplicative scaling for each channel, which again can vary with different range index settings but tend not to. Finally, multi-bunch running requires correction for the crosstalk

between a signal in a particular channel in a particular bunch and that same channel in subsequent bunches. This is due to time structure of the amplified signal, which includes an overdamped return to the baseline that needs ~ 10 ns in order to settle. Bunch-to-bunch crosstalk is largest for 4 ns bunch spacing, the smallest spacing available at CESR-TA.

Mean pedestal values and associated Gaussian widths (which are used in image error bars) are obtained by reading out the detector with circulating beam, but with a closed beamstop, preventing x-rays from reaching the detector. A typical distribution of pedestals observed in detector images and Gaussian fits to them are shown in Fig. 30. Figures 31(a) and 31(b) show pedestal and width values, respectively, vs. channel and preamplifier range index. Gain and range calibrations both require single-bunch data with a wide open optical element, which exposes all 32 channels to substantial radiation that varies smoothly across the detector (see Eq. (6)). For each range, gains are computed from a fit of the images to a Gaussian; a typical detector image and Gaussian fit is shown in Fig. 32 and gain values vs. channel and range index in Fig. 33. The patterns and approximate reflection symmetry about the middle of the detector in both pedestal and gain values vs. channel number reflect the symmetry and characteristics of the physical layout on the readout board. Variation with preamplifier range is small relative to channel-to-channel gain variation. During the gain calibration, images are reviewed for basic structure with an eye towards identifying individual channels which are behaving badly. Such bad channels have typically taken the form of a constant or stuck value, a consistently low or high value or intermittently inaccurate values. Bad channels are identified and diagnosed at the hardware level until all channels are performing reasonably. If electronics components are replaced, channel calibrations are performed again, starting with pedestals.

Range calibration is completed using WO-optic data in all ranges when the single bunch current is large enough to give significant pulse height in all ranges but not so large as to cause saturation on the highest gain range; all ranges are forced by the range correction to yield the same number of corrected counts.

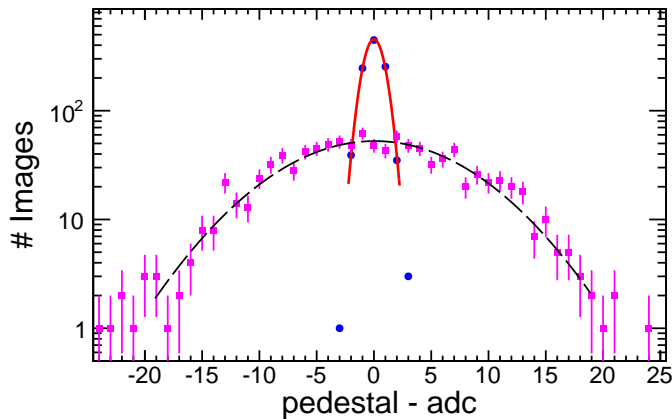


Figure 30: Pedestal distributions for channel #1 on range index #1 (circles and solid line Gaussian fit) and range index #25 (squares and dashed line) in pedestal runs.

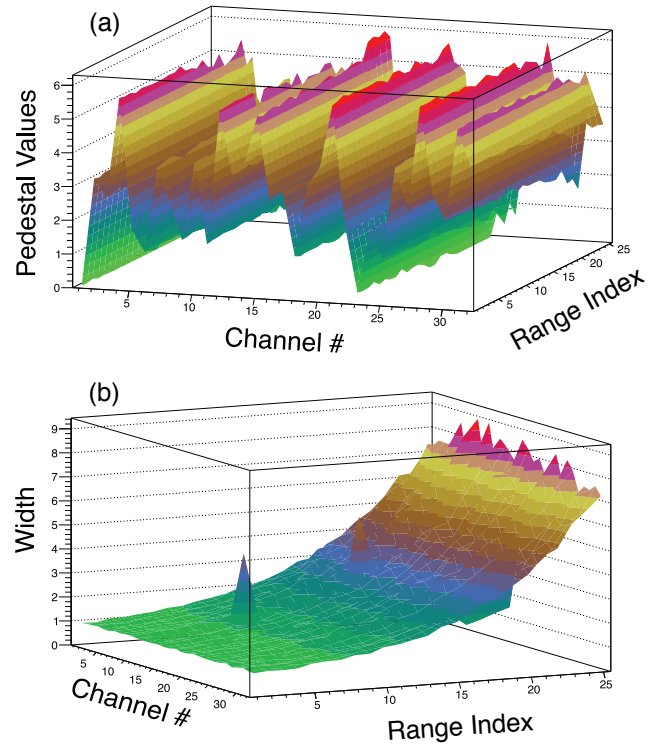


Figure 31: (a) Mean pedestal values and (b) their Gaussian widths, each as a function of channel number and range.

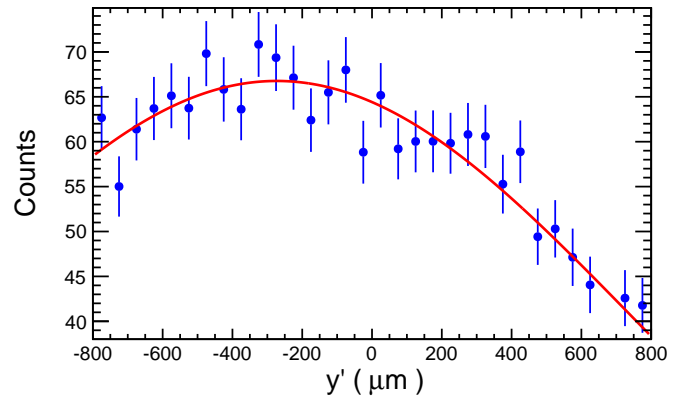


Figure 32: Typical detector image from a gain calibration run for a wide-open optical element and preamplifier range index #1. The solid line is a Gaussian fit to the data, which have already undergone a few iterations of calibration.

For amplifiers on both beamline installations the final range calibration finds that each step in index indicates a gain change of 11.9% instead of the nominal 12.2%, with a maximum deviation of any individual range from that average step size of $\sim 1.3\%$, as shown in Fig. 34.

The bunch-to-bunch crosstalk correction also requires a special type of data collection, one in which CESR is configured to run and trigger data collection with multiple bunches but only the first is filled with electrons or positrons. This dataset is accumulated with the wide-open optic. Each channel's correc-

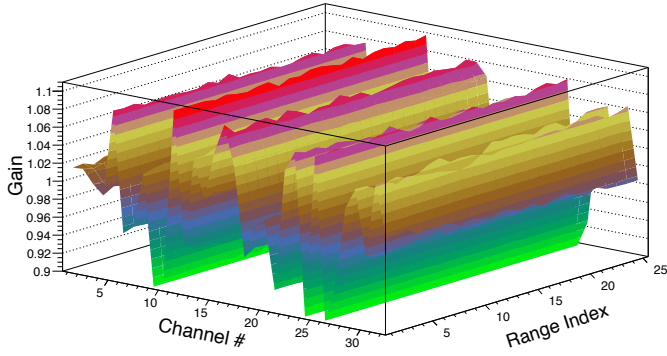


Figure 33: Gain values for all channels and ranges.

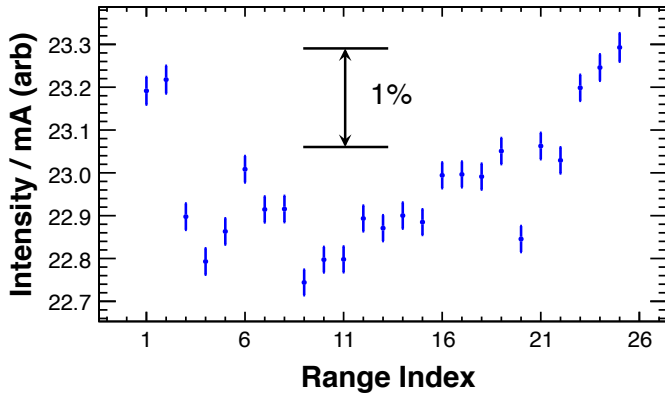


Figure 34: Peak intensity per mA of beam current vs. preamplifier range index for the D-line xBSM installation. Ideally all data points should be consistent with the same fixed value; their spread shows the $\sim 1\%$ variation across the full dynamic range.

tion for a particular follow-up bunch is the fraction of the first bunch's pulse height that is recorded there, after correcting for pedestal, gain, and range. Bunch-to-bunch crosstalk corrections are then applied to true multi-bunch data by adjusting pulse height in a particular channel in a particular bunch to compensate for crosstalk from the preceding bunches' pulse heights. As shown in Fig. 35, the correction can be in the 20-30% range for the next bunch in 4 ns bunch-separation data, and significant residual signals persist for several more bunches, whereas for 14 ns bunch-separation data the correction even for the first succeeding bunch is $\sim 1\%$.

After the timing values have been tuned and calibrations performed, the instrument is deemed ready for experimenters.

4.5. Setting the pinhole opening

The prf for any optical element depends on the gap size, and the optimal gap size for a pinhole depends upon the x-ray spectrum. As the x-ray spectrum varies with the beam energy, the pinhole opening must be reset for each change of E_b , or upon initial setup each run period. The motors controlled actuator determining the pinhole opening, described in Sect. 3.3, has digital setpoints that are nearly linear in the gap size. However, the zero-opening setpoint can vary between run periods, so confirmation of the actual opening is performed using images from

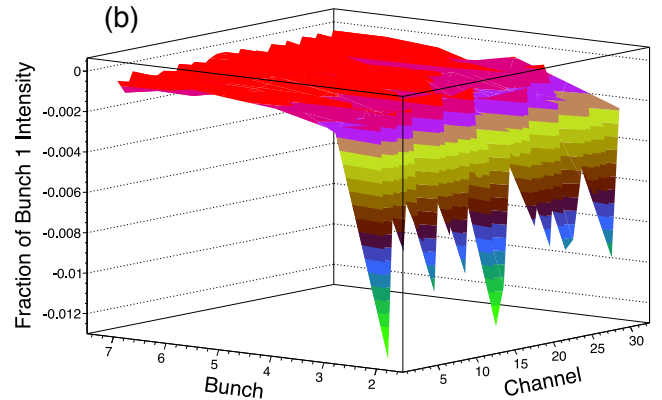
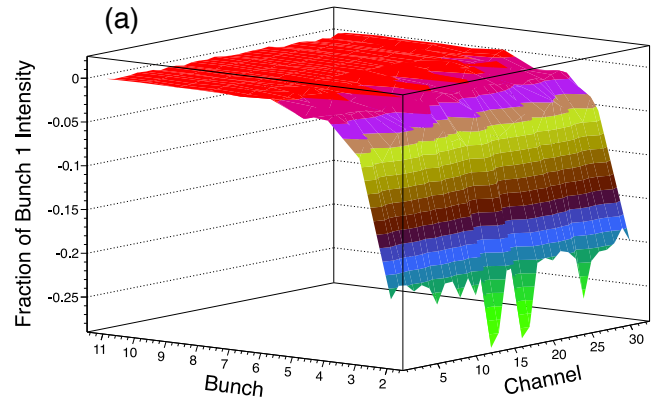


Figure 35: For a multi-bunch fill with bunch separations of (a) 4 ns, or (b) 14 ns and current only in bunch #1, the pulse height in each detector channel measured for succeeding bunches as a fraction of the corresponding value in bunch #1, plotted vs. channel and bunch number.

the data at different actuator settings. The desired setting is that which minimizes the fwhm of the measured image. While the optimal gap size is known from modeling studies of resolving power to be about ten microns wider than where the minimum width occurs, the minimum image width setting is more robust in fitted beam size with respect to small changes in pinhole gap size, and hence a reliable calibration point. Further information on pinhole opening studies appear in Sect. 5.3.

5. Results

5.1. Detector spectral response

Precision fitting of images requires an accurate prf. To do so, in addition to knowledge of the geometry, optical element specification, beam energy, and filtering, one needs to know the effective spectral response of the detector, at least to the extent that it is not uniform in wavelength. This includes the energy-dependent attenuation of any coatings in front of the active material as well as the absorption of the diode itself, including the degree to which absorption of x-rays translates into pulse height. As a nominal starting place we can account for the $0.16 \mu\text{m}$ of Si_3N_4 specified as the passivation layer and assume 100% efficiency of transmitting energy absorbed in the InGaAs

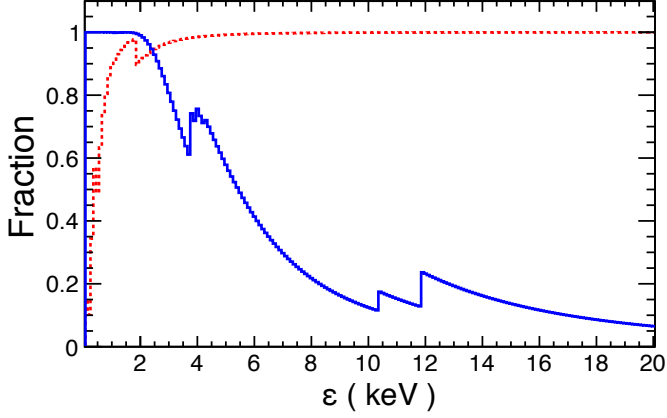


Figure 36: Predicted x-ray absorption of the InGaAs detector (solid histogram) and transmission for the Si_3N_4 passivation layer (dashed histogram) as a function of energy.

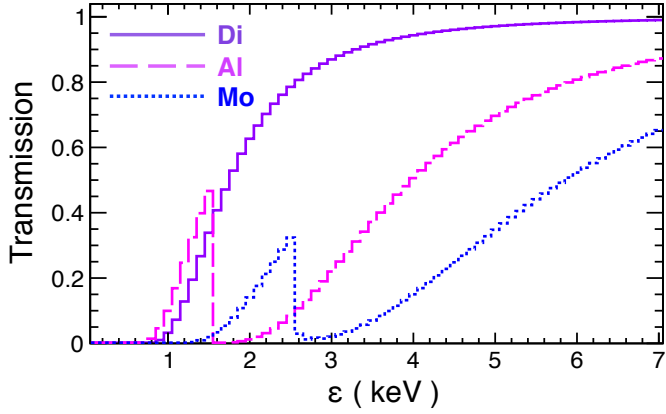


Figure 37: Filter transmission curves as a function of x-ray energy for the diamond (solid), aluminum (dashed), and molybdenum (dotted) filters, using thicknesses specified in Table 3.

into detected photoelectrons, as shown in Fig. 36. Note the two general features that inactive material will inhibit the lowest energy x-rays from reaching the active part, and that the ability of the active portion to absorb incident radiation decreases steadily above 2 keV (aside from modest dips and spikes from photoelectric absorption edges).

We determine the effective spectral response empirically because the idealized assumptions do not account for the conversion of absorbed energy into detected charge, and because specified layer thicknesses may be inaccurate. A laborious but effective technique to do so has been developed. It relies upon the fact that our three different filters probe different portions of the spectrum. We compare the image areas per unit beam current in pinhole images with filters upstream of the detector to those without any filter present. Gathering such data at four different beam energies enables a detailed description over the range of important wavelengths. The method has sensitivity for two reasons: first, because the underlying spectrum shifts upward for increasing beam energies (as shown in Fig. 1), thus highlighting different parts of the x-ray spectrum; and second, because each of the filters highlights a different energy range

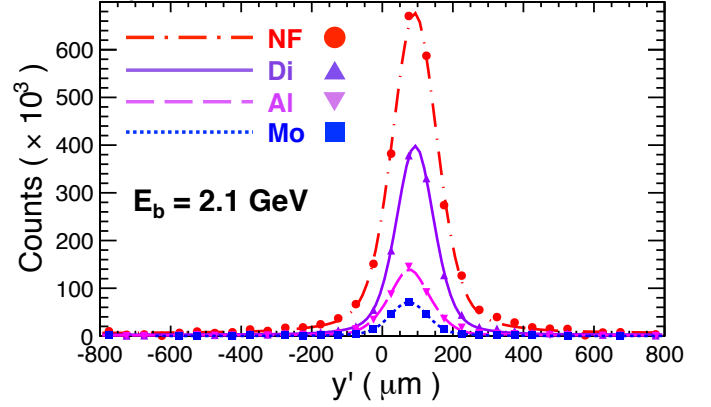


Figure 38: Detector images taken with the pinhole optic and corresponding fits at $E_b = 2.1$ GeV with different filters in place, as indicated. The images shown represent sums over 1024 turns.

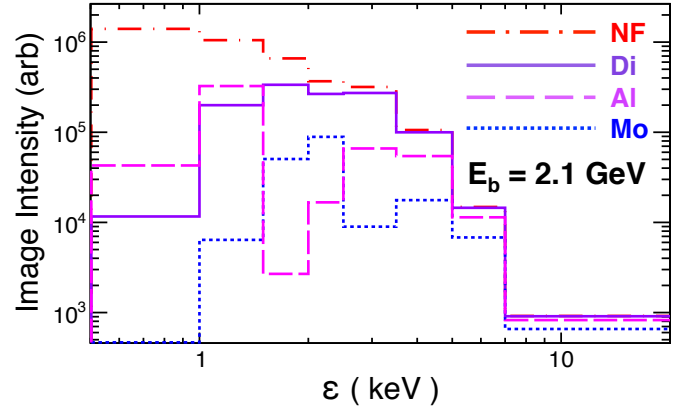


Figure 39: Contributions to prf areas from different x-ray energy bins for $E_b = 2.1$ GeV and different filters, as indicated.

(as shown in Fig. 37). We use ratios instead of absolute intensities to avoid systematic issues associated with retuning the x-ray beam trajectory at different beam energies.

Data accumulation and analysis proceed as follows:

- At each of the four beam energies, with the diamond filter in place, set the pinhole opening to the value which minimizes the fwhm of the image. Maintain this gap for all four different filter runs at each beam energy.
- Accumulate at least 1024 turns of single-bunch images with each of four filter configurations: no filter (NF), diamond filter (Di), molybdenum filter (Mo), and aluminum filter (Al). The beam current is recorded with each dataset for use in the next step.
- Using a given spectral response⁷, build prfs for each beam energy and filter. Then fit the measured images from each dataset to the appropriate prf for beam size, beam position, intensity, and a floating flat background term to ac-

⁷Initially, assume the nominal materials and a flat response; later, use the result of the previous iteration. The analysis converges after a single iteration.

count for uniform pedestal shifts. Tabulate the average intensity per turn per unit current for each beam energy and filter.

- Form three ratios of intensities/turn/mA for each beam energy: Di/NF, Mo/NF, and Al/NF. Assign systematic uncertainties from variations observed from data taken at different times with different currents, which amount to 1-3% for each numerator and denominator.
- Perform a χ^2 -minimization fit of the twelve intensity ratios to 11 or fewer floating parameters, each of which determines the relative strength of a different photon energy bin within the range 0-20 keV. In the fit, each strength parameter multiplies a corresponding energy bin of the spectrum obtained from Eq. (3). At least one photon energy bin's strength must remain fixed in order to set a scale for the others; this procedure only determines a shape of the spectral response. We choose the nine energy bins shown by the points with error bars in Fig. 41, holding the 2.5-3.5 keV bin's strength fixed at a value of 1.0. (X-ray energies above 7 keV only contribute modestly at $E_b = 2.6$ GeV, and are not significant at lower E_b .)

Complete datasets at four beam energies were accumulated on CESR's D-line (e^+) xBSM station. Results are given for the second iteration of analysis. Representative images and fits are shown in Fig. 38. Contributions to the areas from different x-ray energy bins are shown in Fig. 39.

The fit is not guaranteed to give physical results, and could potentially chase down an artifact where χ^2 is slightly smaller than the "right" answer. These issues are dealt with by constraining the energy bin strengths to all be positive, and to require that these strengths fall as x-ray energy increases above 4 keV, as must occur due to the absorption capability of the InGaAs detector. The initial unconstrained fit gives a negative result for the 0.5-1 keV bin and a value greater than 1 for the 7-20 keV bin; both are unphysical and have large uncertainties. Hence we fix the value of the 0.5-1 keV bin to be 0.05, a small but reasonable value consistent within 1σ of the initial result. We fix the value of the 7-20 keV bin to be 0.3 so as to be consistent with a physical response that falls with increasing energy; it will be shown later in Sect. 5.4.7 that even large variations in this value have virtually no effect on beam size.

Results of the fit to the data as described are shown in Figs. 40 and 41. The fit has a reasonable $\chi^2 = 4.9$ for six degrees of freedom. The histogram in Fig. 41 represents the piecewise-linear model of detector response (*i.e.*, the spectral response function $S_d(\epsilon)$ in Eq. (10)) used in constructing point response functions. Contributions to a pinhole prf from different x-ray energy bins at $E_b = 2.1$ GeV, assuming the piecewise-linear detector response and the diamond filter, are shown in Fig. 42. It is evident that the shape of this prf is determined dominantly from x-ray energies in [1.5-5.0] keV, and therefore mostly depends upon just three of the bins other than the normalization bin, 2.5-3.5 keV, two lower and one higher. This remains true at all beam energies from 1.8-2.6 GeV, making the physicality assumptions in the filter scan fit at very low and very high x-ray

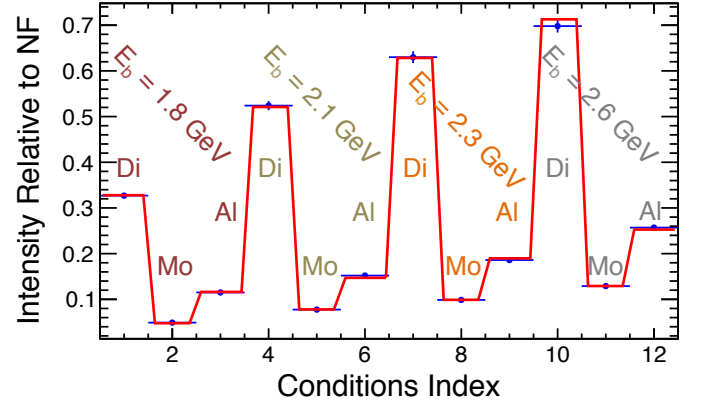


Figure 40: Filter scan fit of intensity relative to the NF data vs. the conditions index, which cycles through beam energy/filter combinations as indicated. Solid circles represent the data and the histogram the best fit.

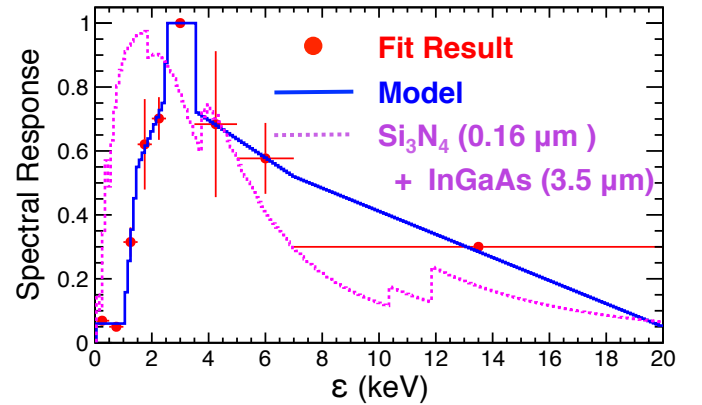


Figure 41: Fit results for the relative detector response as a function of x-ray energy (solid circles with error bars), a piecewise-linear model used for constructing prfs (solid line), and the curve predicted (dotted line) using the nominal materials and thicknesses in the detector.

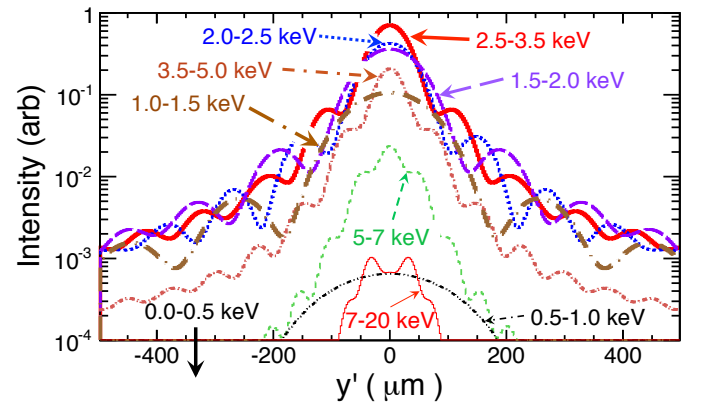


Figure 42: Contributions segregated by x-ray energy bin, as indicated, to the pinhole-optic prf for $E_b = 2.1$ GeV with the diamond filter assuming the detector response of the piecewise-linear model of Fig. 41.

energies of little but cosmetic import.

Estimating systematic uncertainties in the prfs from the error bars of the fit requires some care due to substantial bin-to-bin fluctuations. For example, fixing the strength of the 2.0-

2.5 keV bin to a value 1σ (10%, relative) larger than the final fit results in the best-fit value for 1.5-2.0 rising by 15% (relative) and 3.5-5.0 keV by about 26% (relative). Such correlations are fortuitous for stability of beam size with respect to spectrum uncertainty because the higher energy bin contributes a narrower component to the prf, and the lower energy bins a broader component, so that overall, in this example, the prf shape is only very slightly altered. Quantitative estimates of systematic uncertainty on beam size from spectral response uncertainty is explored in Sect. 5.4.7.

5.2. Beam size extraction

Each image in a data run is subject to a χ^2 -minimization fit to a template appropriate for the beamline geometry, optical element, beam energy, and filters in use for that run, with the fit parameters being the amplitude A_b , the beam offset y_b , the beam size σ_b , and a flat background term. To properly weight each of the 32 pixels in the fit, each point must be given reasonable uncertainties. We assign the uncertainty to be the quadrature sum of three terms: one for the least-count effects on the gain range being used, one for the electronic noise corresponding to the average pedestal width, and one to roughly account for the statistical variation in the number of photoelectrons collected for that pixel. The first is trivial to assign as a single count and the second is derivable from the pedestal width measurements described in Sect. 4.4. The third term is obtained from data taken with a wide-open optic, as shown in Fig. 32; deviations from the Gaussian fit are taken as attributable to the three sources enumerated here, and the statistical portion is taken as that which remains after the other two are accounted for.

We have developed two methods for extracting a beam size that should be applicable to the entire run (typically $N=1024$ -4096 turns) for each bunch. Each method has its advantages and disadvantages. The first technique calculates a *turn-averaged* beam size $\langle\sigma_b\rangle$ by taking a weighted average of the N individual turn image fits, using the statistical uncertainty from each turn's individual fit (inflated by the factor $\sqrt{\chi^2/\text{dof}}$ if that factor exceeds unity). Because failed fits on a small number of turns can give results which skew a weighted mean, outliers beyond three standard deviations from the mean are excluded in two iterations involving recalculation of the standard deviation

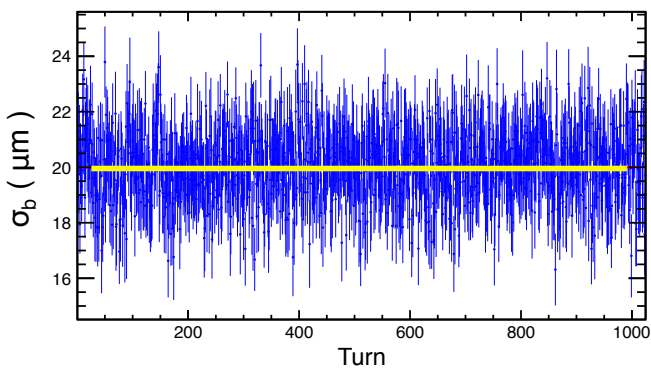


Figure 43: Beam size vs. turn for a run of 1024 turns. The solid line represents $\langle\sigma_b\rangle$, the weighted average, excluding outliers, of the 1024 measurements.

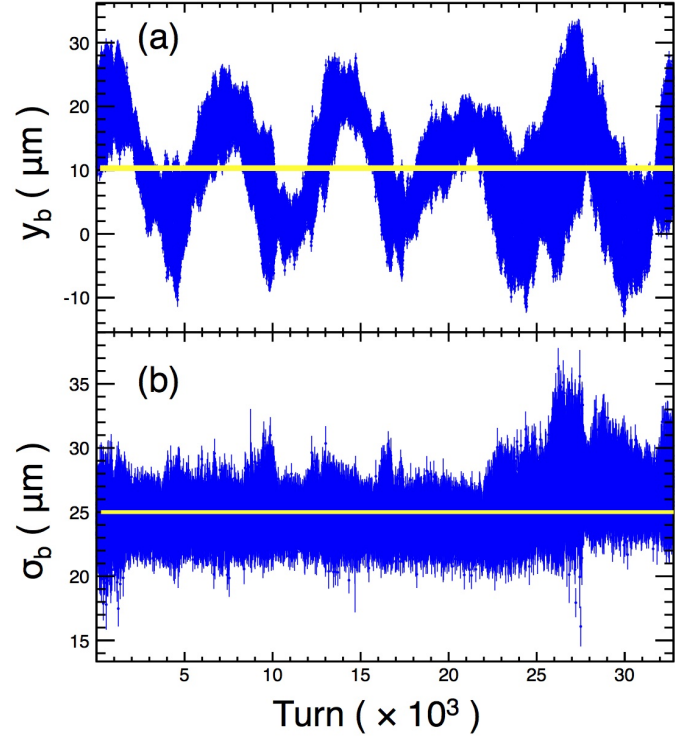


Figure 44: (a) Beam position and (b) beam size vs. turn for a single bunch run of 32768 turns. Each solid horizontal line represents the weighted average over all turns, excluding outliers. There is visible variation, beyond that expected from statistics alone, in both beam position and beam size as a function of turn.

after each. This method is quite robust when there is sufficient pulse height on each individual turn so that the turn fits are reliable. An example of a successful $\langle\sigma_b\rangle$ extraction is shown in Fig. 43. Outlier rejection is applied to all fitted parameters when reporting turn-averaged quantities.

The turn-average method can break down at very low current when the number of bad fits, and hence outliers, becomes large. We have also observed that, at low current and using the pin-hole optic, this method gives a beam size that is biased low by up to several percent. This effect is not fully understood, but is thought to be attributable to cases where most pixel signals correspond to fewer than 20 photoelectrons, which will obey Poisson rather than Gaussian statistics, and which will be more strongly affected by least-count digitization effects. This effect was observed by comparing the beam size for a given moderate current run with no attenuator with that obtained just after attenuator insertion (which limited the horizontal detector exposure, thereby reducing flux onto the detector). The effect appears in the attenuated data near 0.5 mA/bunch and grows as current decreases.

Hence we developed a second method of computing beam size from turn-by-turn data; it yields a quantity we call the *corrected image-summed* beam size, Σ_{bc} . Here we treat all the turns for each bunch as a collective that has several relevant properties:

- Σ_b , the image-summed beam size obtained by simply adding all turn images together before fitting to a template;

- σ_{y_b} , the rms beam motion for the run, obtained from the turn-by-turn y_b values; and
- δy_b , the median statistical error, on the turn-by-turn values of y_b .

In the limit of zero beam motion, the image-summed beam size Σ_b matches the turn-averaged beam size Σ_b at moderate or high currents. However, frequently there can be substantial vertical beam motion, so that a correction to the naive image-summed beam size is necessary. The correction first subtracts the rms beam position σ_{y_b} in quadrature, but then adds back the median statistical error on beam position δy_b (again, in quadrature) so as not to bias the result by a purely statistical nonzero value of σ_{y_b} . Summarizing:

$$\Sigma_{bc}^2 \equiv \Sigma_b^2 - \sigma_{y_b}^2 + (\delta y_b)^2 . \quad (18)$$

For moderate to high current runs, $\Sigma_{bc} = \langle \sigma_b \rangle$ to within a small fraction of a micron, regardless of beam motion. At low energy and/or low current, however, Σ_{bc} is slightly larger than $\langle \sigma_b \rangle$, although only enough to reduce but not eliminate the low-current bias. In the remainder of this section, the beam size quoted will be the turn-averaged value, $\langle \sigma_b \rangle$, because we will not be showing very low current data.

We have also observed that values of either type of beam size can vary by $\sim 1 \mu\text{m}$, outside their statistical errors for 1024-turn (or fewer) measurements, taken just seconds apart on the same CESR fill. One source of such variation is feed-through of low frequency noise (*e.g.*, AC line voltage) into CESR bending and focusing magnets, which operate on tightly regulated DC current. This becomes apparent for some running conditions if one takes runs of, *e.g.*, 32768 turns, as seen in Fig. 44. When comparing beam size measurements of the same CESR fill using data taken with 1024 (or fewer) turns, several runs (if available) need to be combined in order to average over such effects; additional data was not always taken, so statistical uncertainties in 1024-turn beam sizes are not representative of deviation from the average over longer time scales.

5.3. Optical element models

Measured beam size depends upon the prf, and the prf depends upon the model, where by “model” we mean the assumptions made when computing the prf. As described in Sect. 2.2, we choose to make all computations in the yz plane, ignoring the horizontal, due to the symmetry of the setup. Geometrical quantities, shown in Tables 3-6 are reasonably well-known from direct measurement and/or specifications of manufacturers. Effects of filters, optic substrates, and masking are taken from the nominal compositions and thicknesses and material properties catalogued in [34]. The spectrum from Sect. 5.1 is used, along with all the geometrical and material information, in Eq. (9). A step size of $0.1 \mu\text{m}$ is used along the optical element height, and prf values are computed every $2.5 \mu\text{m}$ along the image plane; both of these step sizes are finer than necessary. The coded aperture prf is completely determined from these parameters.

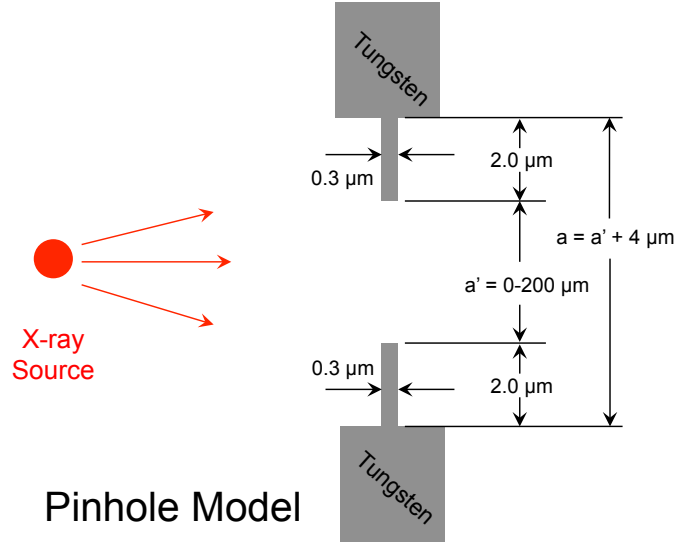


Figure 45: The adjustable pinhole model for prf generation (see text).

The adjustable pinhole, however, presented a challenge in two respects. First, the separation of the blades, while reproducible through motor settings, must be calibrated to an absolute scale. Secondly, we found that allowing for μm -level imperfections in the machined blade surfaces only narrows the single-peaked prf relative to a no-roughness model (this is similar to the effects of masking on single-slit optical elements discussed in Sect. 2.5). Hence we adopt a roughness model to generate prfs that are in the “middle” of the range of roughnesses that are possible. From the discussion in Sect. 2.5, it becomes apparent that x-rays passing through any tungsten on their way to the target will affect the prf in a similar manner as does the gold masking on a coded aperture. So our model, shown in Fig. 45, has two parameters: the width of a uniformly thick tungsten lip on each edge of the pinhole opening, and a thickness of this lip. If this lip is very thick ($> 1 \mu\text{m}$), it cannot substantially affect the prf because the lip region transmits virtually no light. Conversely, if it is very thin ($< 0.05 \mu\text{m}$), it introduces a phase shift which is too small to matter, except insofar as the lip width increases the effective gap between the blades (and which will be included in the calibration described below). We chose an effective tungsten lip thickness of $0.3 \mu\text{m}$ as a value which introduces a substantial phase shift but transmits enough light for it to affect the prf. This then allows the lip width to be the single parameter in the model which controls effects of partially transmitting material. Our model must assume some nonzero lip width on each side, at a value where the narrowing of the prf is roughly midway between the no-lip and the widest credible lip in the context of this model. We found this midway point to be a lip width of $2 \mu\text{m}$ on each side of the opening; this width narrows the prf by about 6% relative to the no-lip case.

What remains is to calibrate the pinhole motor setting to an absolute gap size in our model. This calibration has the following steps:

1. The model is verified to yield a predicted image area that

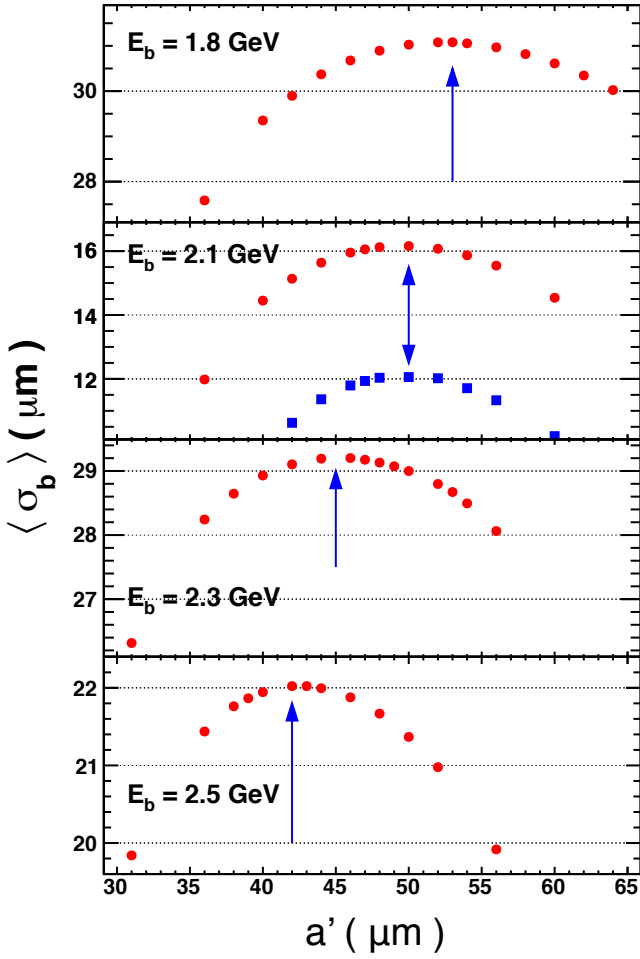


Figure 46: Turn-averaged beam size from e^+ beam data taken with the diamond filter and the optimized pinhole optic vs. pinhole gap size used to generate the template used to fit each point, for four beam energies (see text). Each set of solid squares or circles corresponds to data from the same run at that beam energy, but fitted with different prf-based templates. The arrows indicate the maxima of each distribution.

varies linearly with opening for gap sizes above $10 \mu\text{m}$. The dependence is seen to be that the size a' , shown in Fig. 45, depends on the relative image amplitude (area) A_b as

$$a'(\mu\text{m}) = 50.6 \times \frac{A_b}{A_b(50 \mu\text{m})} - 0.6. \quad (19)$$

Thus, the two $2\text{-}\mu\text{m}$ -wide tungsten lips in our pinhole model correspond to an unobstructed opening of $0.6 \mu\text{m}$ in transmitted x-ray intensity.

2. The model is used to determine, for each beam energy and assuming use of the diamond filter, the absolute gap size corresponding to the narrowest prf. This has been done in two different ways that obtain consistent results. In one method, each predicted prf is fit to an *ad hoc* but conveniently analytic function with one floating parameter that controls its width. The function used is a double Gaussian with both components constrained to the same mean, one component with a narrow width σ_N accounting for 80%

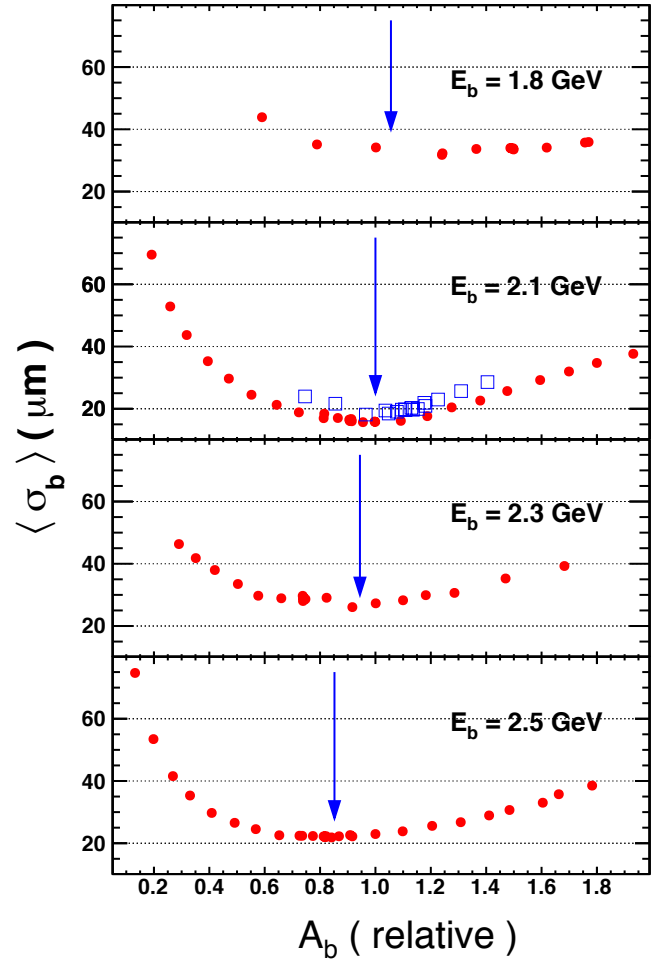


Figure 47: Turn-averaged beam size from e^+ beam data taken with the diamond filter vs. relative image area taken in the scan to optimize the pinhole optic opening, for four beam energies (see text). The arrow locations are placed so as to preserve the relative openings found in Fig. 46, and can be seen to point to the minimum total width of the observed pinhole image at each beam energy.

of the area and a second with a broader width σ_B , where $\sigma_B \equiv (100 \mu\text{m})^2 + \sigma_N^2$, accounting for the remaining 20%. The optimal gap size is that which yields a prf with the smallest σ_N . The second method looks at a data run taken at the same beam energy. A run with small beam size is chosen so as to obtain the best sensitivity. This same run is fit to templates based on prfs generated with different gap sizes; by definition, the narrowest prf occurs where the largest beam size is obtained. Results from this latter method appear in Fig. 46 for all four beam energies. Note that two different runs with different beam sizes at $E_b = 2.1 \text{ GeV}$ both result in maxima at the same gap of $50 \mu\text{m}$, and that all maxima are determined to within $\sim 1 \mu\text{m}$. The narrowest images when using the diamond filter are obtained for model gap sizes of $53, 50, 45,$ and $42 \mu\text{m}$ for, respectively, $E_b = 1.8, 2.1, 2.3,$ and 2.6 GeV .

3. The motor setting was measured to have linear dependence upon the corresponding fitted amplitude A_b per unit beam

current, locally in the vicinity of the minimum prf width, with reproducible slope and intercept on a given CESR fill. Since the prf has unit normalized area, A_b corresponds to area, which, from item (1) above, corresponds to a particular motor setting.

4. For each beam energy, runs are taken over a range of pinhole motor settings on the same CESR fill just minutes apart, and the fitted σ_b and A_b per unit beam current recorded for each using templates from a single prf for all data at that beam energy (it does not matter exactly what gap size was used for the prf, as this step is not determining absolute beam size). The values of fitted A_b per unit current are then scaled to that obtained for the motor setting known to give the narrowest image at $E_b = 2.1$ GeV. The resulting data are shown in Fig. 47. Two separate datasets are shown for $E_b = 2.1$ GeV. The arrow position shown are fixed in relative amplitude to those obtained from Fig. 46, establishing a consistency between the model and the data. Since each value of relative amplitude per unit current is known to correspond to a particular motor setting, this allows a calibration of motor setting to model gap size.

5.4. Systematic uncertainty in beam size

While sensitivity of some sources of uncertainty in beam size can be investigated from first principles (*e.g.*, statistical sensitivity in Sect. 2.5) or models (*e.g.*, pinhole roughness in Sect. 5.3), others must be addressed with measurements. We use data for this purpose in two ways. First, we can quantitatively examine how a particular parameter, P , alters the beam size in a given dataset as it varies around its likely value and induces changes in the prf. With this technique one can determine whether the data are *self-calibrating* in each such parameter, and what the effect of changing P is on measured beam size. If the data are self-calibrating, the actual value, P_0 and its uncertainty ΔP can be extracted from the data and no nominal or specified value for that parameter is needed; if the data are not self-calibrating, reliable separate specifications of P_0 and ΔP are required. In either case, $d\sigma_b/dP$ in the vicinity of P_0 can be extracted from the data, and the systematic uncertainty taken as $d\sigma_b/dP \times \Delta P$. This use of data is quite effective, as the same data are used for each parameter setting, meaning any variation in fit quality or beam size is in fact due to the parameter value change. With this method, we will describe tests of the sensitivity of beam size to

- the magnification, by varying it;
- the pinhole roughness model, by varying the lip width;
- the coded aperture model, by varying the slit widths;
- the coded aperture model, by varying the gold masking thickness;
- the prf approximation for a misaligned optical element, by varying the detector offset d as defined in Eq. (13);

- the predicted spectrum, by varying the assumed spectral response;

In the second method for determining sensitivity of measured beam size to various sources of uncertainty, we compare data taken in different experimental conditions during a given CESR fill with stable beam size. Under the assumption that the beam size does not change in the several seconds or minutes between measurements, stability of beam size with respect to the particular change can be studied. One obstacle limiting the precision of such tests is that up until now, many, but not all, data runs contain only 1024 turns each, and so are subject to true beam size oscillations at low frequency. These oscillations are not always present, but are not easily detectable without runs containing 8192-32768 turns (as seen in Sect. 5.2 and Fig. 44). Such beam size variations are frequently of magnitude $\sim 1 \mu\text{m}$ or larger. Sometimes this effect can be mitigated by combining several 1024-turn runs taken in essentially identical conditions. (For future operations, we plan to increase the standard number of turns from 1024 to at least 8192). With this technique, we will describe beam size dependence upon

- the pinhole model, by varying the gap size;
- the predicted spectrum and spectral response, by using different filters and/or different beam energies; and
- the overall systematic uncertainty of pinhole and coded aperture models, by changing optical element from one to another in various conditions.

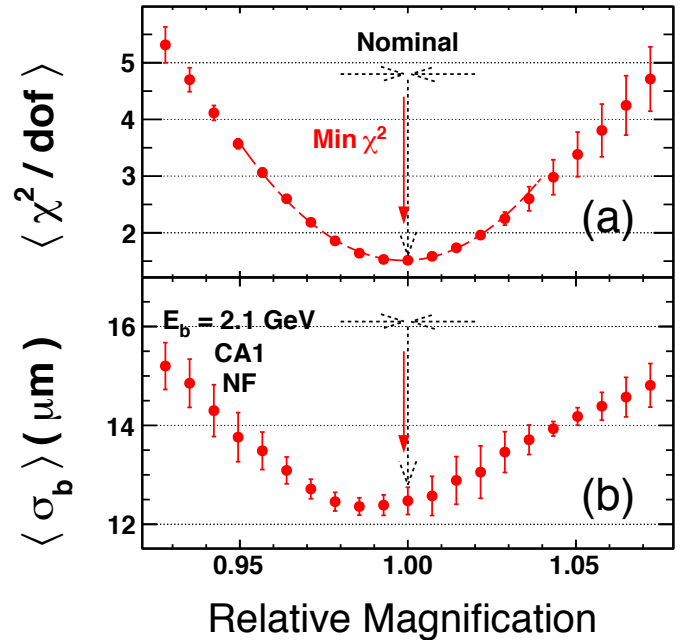


Figure 48: From coded aperture e^+ data for $E_b = 2.1$ GeV with no filter, turn-averaged (a) χ^2/dof and (b) beam size as a function of the magnification applied to the fits; *i.e.*, the same data but different magnifications are used for each point. The vertical arrows indicate the nominal and approximate best-fit magnifications as determined from a quadratic fit to $\langle \chi^2/\text{dof} \rangle$ as shown by the dashed curve. Horizontal arrows indicate a span of $\pm 0.1\%$, the nominal magnification uncertainty.

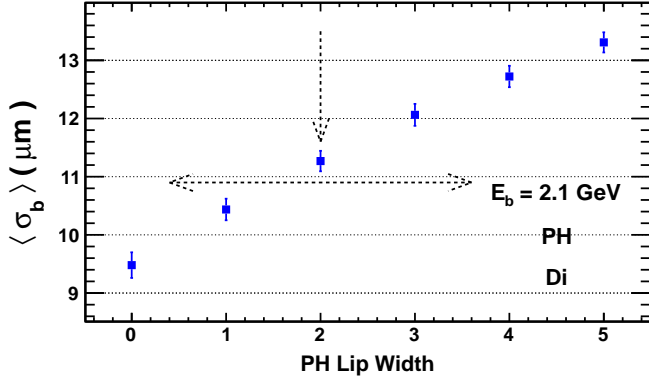


Figure 49: From pinhole e^+ data for $E_b = 2.1$ GeV with the diamond filter, turn-averaged beam size as a function of the lip width used in the prf; *i.e.*, the same data but different lip widths are used for each point. The vertical arrow indicates the nominal value. The horizontal arrow indicates a span of $\pm 1.6 \mu\text{m}$, the estimated uncertainty.

We will show the results of such tests, but due to the aforementioned issue, the precision of these tests is generally inferior to that of the first method.

5.4.1. Magnification

Coded aperture image fit quality is sensitive to knowledge of the geometry. Image features at the extreme ends provide this sensitivity; as the magnification is raised or lowered such features expand away from center or contract toward it. Fig. 48 shows both the turn-averaged χ^2/dof and beam size as a function of the magnification assumed in the prf for e^+ CA1 data acquired at $E_b = 2.1$ GeV with no filter. The best-fit value

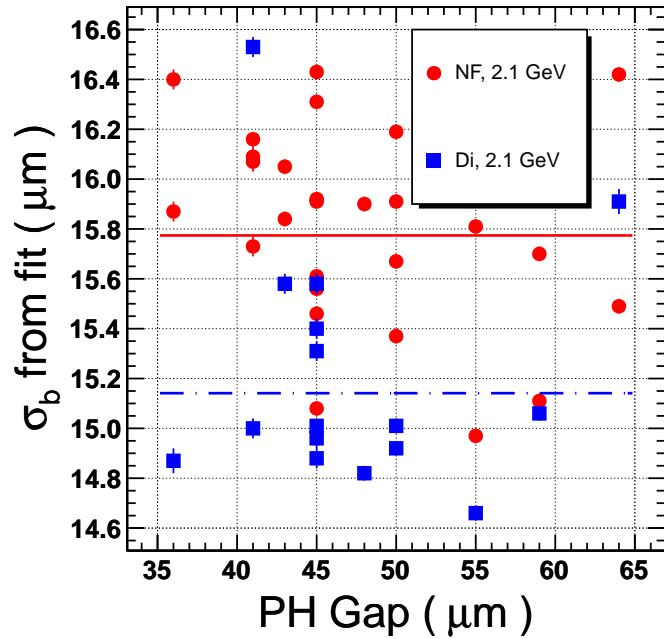


Figure 50: Fitted beam size from e^+ beam data taken with no filter (NF) and the diamond filter (Di) vs. gap size at $E_b = 2.1$ GeV. The solid (dot-dashed) horizontal line represents the mean beam size of the NF (Di) data.

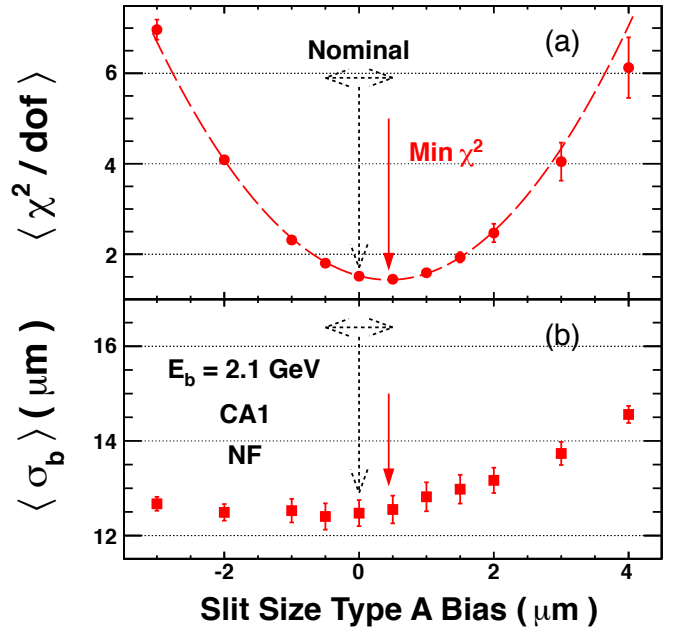


Figure 51: From coded aperture e^+ data for $E_b = 2.1$ GeV with no filter, turn-averaged (a) χ^2/dof and (b) beam size as a function of a slit size bias (Type A, see text) used in constructing the prf used in the fits; *i.e.*, the same data but different prfs are used for each point. The vertical arrows indicate the nominal (dashed) and best-fit (solid) variations from nominal as determined from a quadratic fit shown by the dashed curve in (a). Horizontal (dashed) arrows indicate the nominal uncertainty of $\pm 0.5 \mu\text{m}$.

is 0.12% smaller than nominal, slightly outside the uncertainty quoted in Table 3. Using the nominal 0.1% as the uncertainty in magnification induces a beam size uncertainty for pinhole data of 0.1% at any beam size because the prf is single-peaked. For the CA1 optical element, the same magnification uncertainty induces a beam size uncertainty of $\sim 0.03 \mu\text{m}$ at $\sigma_b = 12 \mu\text{m}$, or 0.3%; sensitivity to magnification decreases at larger beam sizes because the image features become washed out. Hence, unlike the pinhole, relative beam size error for coded aperture measurements due to magnification uncertainty tends to shrink rather than grow with beam size.

5.4.2. Pinhole lip width

Figure 49 shows the variation of beam size with the width of the tungsten lip in the pinhole roughness model. We estimate a systematic uncertainty in this of $\pm 1.6 \mu\text{m}$, for which measured beam size is expected to change by about $\pm 1.33 \mu\text{m}$ at $\sigma_b \approx 12 \mu\text{m}$ and $E_b = 2.1$ GeV

5.4.3. Pinhole gap opening

The pinhole gap calibration method described in Sect. 5.3 results in sensitivities to beam size shown in Fig. 46. It is apparent that sensitivity increases quickly as the PH gap moves away from that which minimizes the width of the prf. For purposes of estimating the relevant sensitivity from Fig. 46, we assume that on average the setting is $\sim 10 \mu\text{m}$ from the optimal one, but that the calibration of Sect. 5.3 specifies the setting within

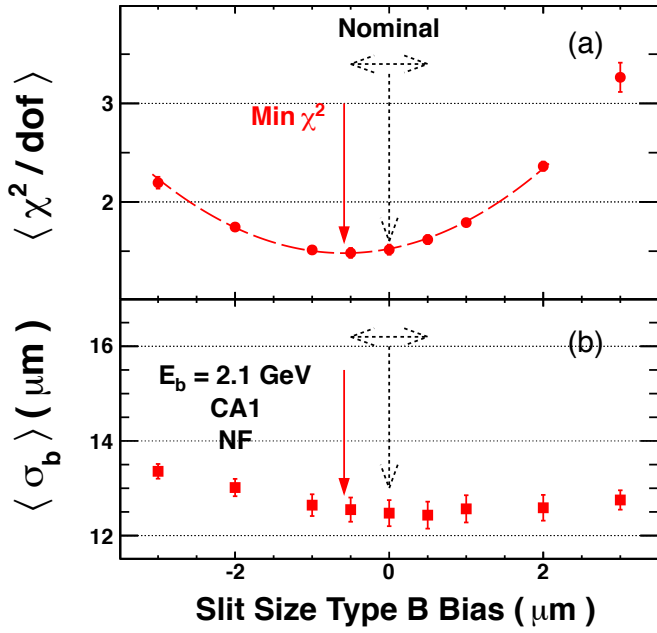


Figure 52: From coded aperture e^+ data for $E_b = 2.1$ GeV with no filter, turn-averaged (a) χ^2/dof and (b) beam size as a function of a slit size bias (Type B, see text) used in constructing the prf utilized in the fits; *i.e.*, the same data but different prfs are used for each point. The vertical arrows indicate the nominal (dashed) and best-fit (solid) variations from nominal as determined from a quadratic fit shown by the dashed curve in (a). Horizontal (dashed) arrows indicate the nominal uncertainty of $\pm 0.5 \mu\text{m}$.

$\pm 2 \mu\text{m}$. This leads to an assigned uncertainty in beam size at $E_b = 2.1$ GeV and $\sigma_b = 12 \mu\text{m}$ of $\pm 0.60 \mu\text{m}$.

Sometimes production data were mistakenly taken at settings not near the optimal settings. In order to verify that such data remain viable, and to investigate sensitivity to our knowledge of absolute pinhole gap size, data from a scan over various openings were fit with the templates from the prf corresponding to the calibrated motor setting, as described in Sect. 5.3. Such a test is shown in Fig. 50. Variations at fixed gap size show systematic run-to-run beam size variations of $\sim 0.5 \mu\text{m}$, consistent with real changes that can happen in these 1024-turn runs. Where there are at least three runs at a given gap size, their average σ_b agrees with other such data with the same filter (but different gap size) to within less than $0.5 \mu\text{m}$. This falls within the assigned systematic uncertainty. The two filter datasets disagree on average by $\sim 0.6 \mu\text{m}$; since they were taken with the same gap opening, this disagreement cannot be due to uncertainty in the gap setting, but rather must be due to other factors.

5.4.4. Coded aperture slit size

The manufacturer's specified tolerance on CA1 slit size and position is given as $\pm 0.5 \mu\text{m}$. We explore two scenarios, each likely to be more extreme than any actual variations from nominal dimensions: one, Type A, in which all slits are systematically larger than specification by the same amount (with adjacent mask size compensating exactly to preserve overall height of the pattern), and another, Type B, wherein adjacent slits alternate being larger or smaller than nominal (with mask sizes un-

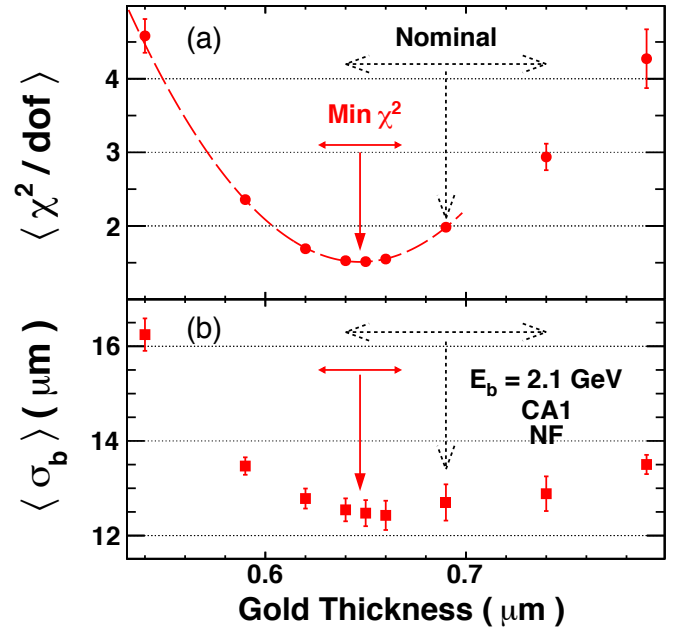


Figure 53: From coded aperture e^+ data for $E_b = 2.1$ GeV with no filter, turn-averaged (a) χ^2/dof and (b) beam size as a function of the gold masking thickness used in constructing the prf utilized in the fits; *i.e.*, the same data but different prfs are used for each point. The vertical arrows indicate the nominal (dashed) and best-fit (solid) thicknesses, the latter determined from the quadratic fit shown by the dashed curve. Horizontal arrows indicate nominal uncertainty (dashed) on thickness from the manufacturer's specification ($\pm 0.05 \mu\text{m}$) and an estimated upper limit on the uncertainty (solid) on self-calibrated thickness.

changed). Figs. 51 and 52 show both the turn-averaged χ^2/dof and beam size as a function of the slit size bias assumed in calculating the prf for e^+ data acquired at $E_b = 2.1$ GeV with no filter. The best fits differ from the specification by $\sim 0.5 \mu\text{m}$; if we use this as the uncertainty on slit size and add in quadrature the change in beam size from the two types of bias, the resulting beam size uncertainty is $0.28 \mu\text{m}$.

5.4.5. Coded aperture masking thickness

The manufacturer's specification on CA1 masking thickness is given as $0.69 \pm 0.05 \mu\text{m}$. Because the mask both attenuates intensity and introduces a phase shift, this level of uncertainty has potential to affect beam size precision. Once again we find that the image fit quality allows the coded aperture to be self-calibrating, this time in gold thickness. Fig. 53 shows both the turn-averaged χ^2/dof and beam size as a function of the masking thickness assumed in the prf for e^+ data acquired at $E_b = 2.1$ GeV with no filter. The best fit differs from the specification by $0.043 \mu\text{m}$. If we use the best-fit value of thickness in the generation of the prf and assume an uncertainty of $0.02 \mu\text{m}$, the resulting uncertainty in beam size is $\pm 0.40 \mu\text{m}$.

5.4.6. Misaligned optical element

When the x-ray source is significantly off-center with respect to the optic, the intensity profile on the optical element becomes asymmetric, and the approximation of Eq. (12) affects the shape of the prf. For such data, it is important to know

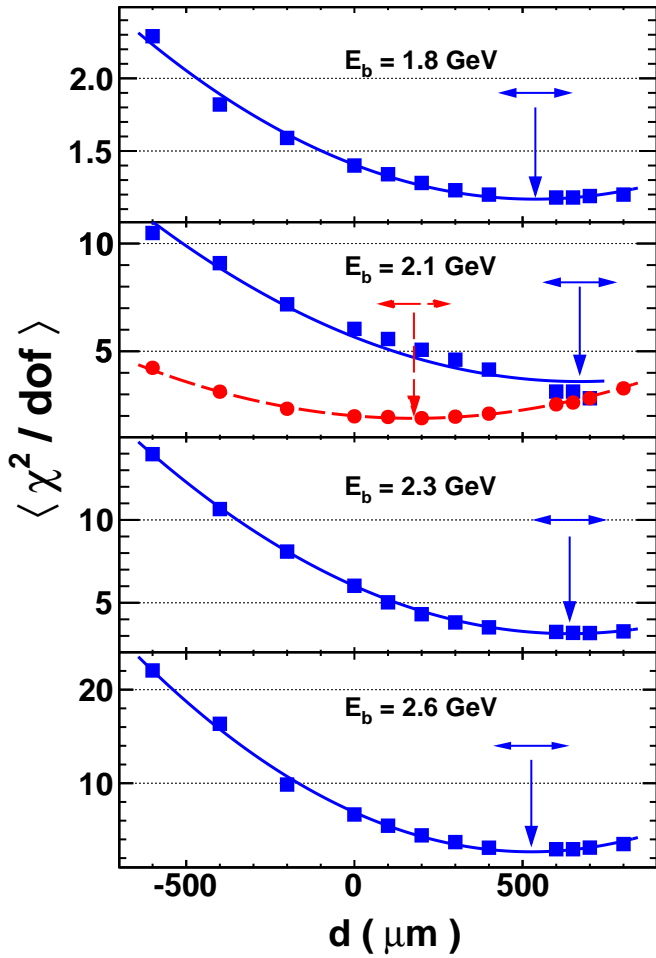


Figure 54: Turn-and-run-averaged χ^2/dof of image fits as a function of the detector offset, d , from the center of the coded aperture that is used to generate templates, for four beam energies and five sets of beam conditions. Curves indicate quadratic fits and vertical arrows the minimum- χ^2/dof location according to the fits. Horizontal arrows indicate a $\pm 100 \mu\text{m}$ span, an estimated upper limit on the d uncertainty from this measurement. The filled circles, dashed curve, and dashed arrows at $E_b = 2.1 \text{ GeV}$ are from a different set of beam conditions than the filled squares/solid curve/solid arrows.

how, if at all, the approximation affects the fitted beam size. Despite attempts to follow the alignment procedures described in Sect. 4.2, several datasets with large vertical offsets (requiring detector offsets $d > 200 \mu\text{m}$, as defined by Eq. (13)) are available. Such runs were discovered in coded aperture data; the signature is significant asymmetry of the fit–data residual on extreme edges of the image. Variations of images acquired with different alignments can be compared. When the pinhole is operated in minimum-prf-width conditions, its opening is small, and there is no significant change in incident intensity over its vertical extent. (This is a positive feature of the pinhole optic: its insensitivity to misalignment.) Conversely, the coded aperture is at least five times taller, and thus, for large d , the variation of intensity from one end to the other can become apparent in the image.

We have found that the value of d is measurable from coded aperture data by examining the dependence of the image fit

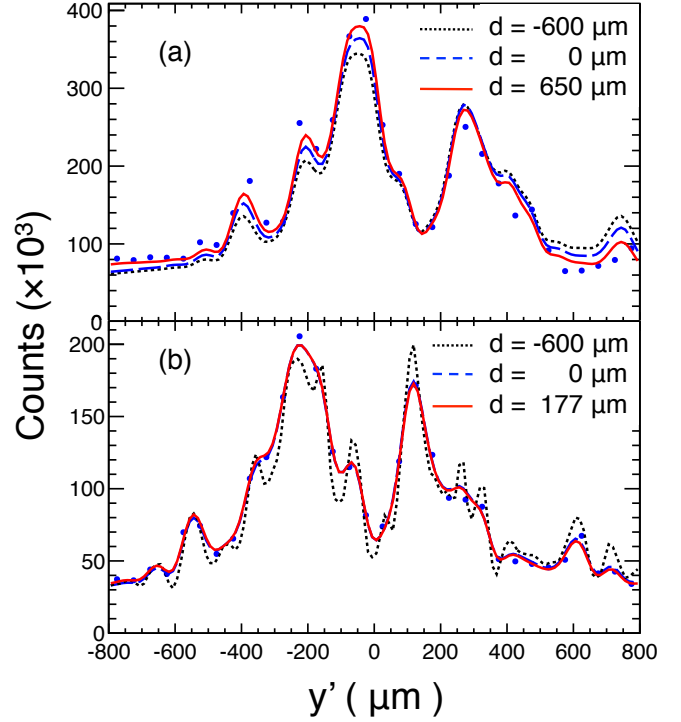


Figure 55: Detector image fits for e^+ two runs taken with different alignments, both acquired at $E_b = 2.1 \text{ GeV}$ with the diamond filter and CA1 optical element. The best χ^2/dof occurs for detector offset (a) $d = 650 \mu\text{m}$ and (b) $d = 177 \mu\text{m}$. Fits for different d values are indicated by curves that are solid (best fit), $d = -600 \mu\text{m}$ (dotted), or $d = 0 \mu\text{m}$ (dashed).

quality, χ^2/dof , on the assumed value of d ; this is shown in Fig. 54 for e^+ data taken at four beam energies. The optimal value of d occurs where the fit quality is minimized, and its uncertainty is determined by its parabolic shape. Variations in image shape attributable to misalignment can be seen in Fig. 55, where the asymmetry induced by the misalignment is apparent. Effects of the approximation in Eq. (12) are visible where the optimal d is large, as in Fig. 55(a), where even the best-fit misses several features in the data. However, for a smaller $|d|$ value, as in Fig. 55(b), the best-fit shape does a much better job of representing nearly every nuance of the image shape.

Using an inaccurate value of d in the fit induces significant variation in the resulting $\langle \sigma_b \rangle$, as shown in Fig. 56, where variation is seen to be approximately linear in d . The value of $\langle \sigma_b \rangle$ for $d = 0$ differs from that for $d = 650$ by 1–2 μm ; to avoid incurring such a bias one must either avoid optic misalignment altogether, or perform this procedure on all coded aperture data (*i.e.*, find and then use the optimal value of d). In the examples of Fig. 54, precisions in optimal d are estimated as $\pm 100 \mu\text{m}$. The uncertainty in beam size due to this uncertainty in d (even for large d) is only $\pm 0.3 \mu\text{m}$.

5.4.7. Spectral sensitivity

The most straightforward test of the spectral sensitivity of measured beam size is to measure the same dataset with each optic with different assumed spectra. Seven alternate spectral response functions were extracted from the filter scan data as

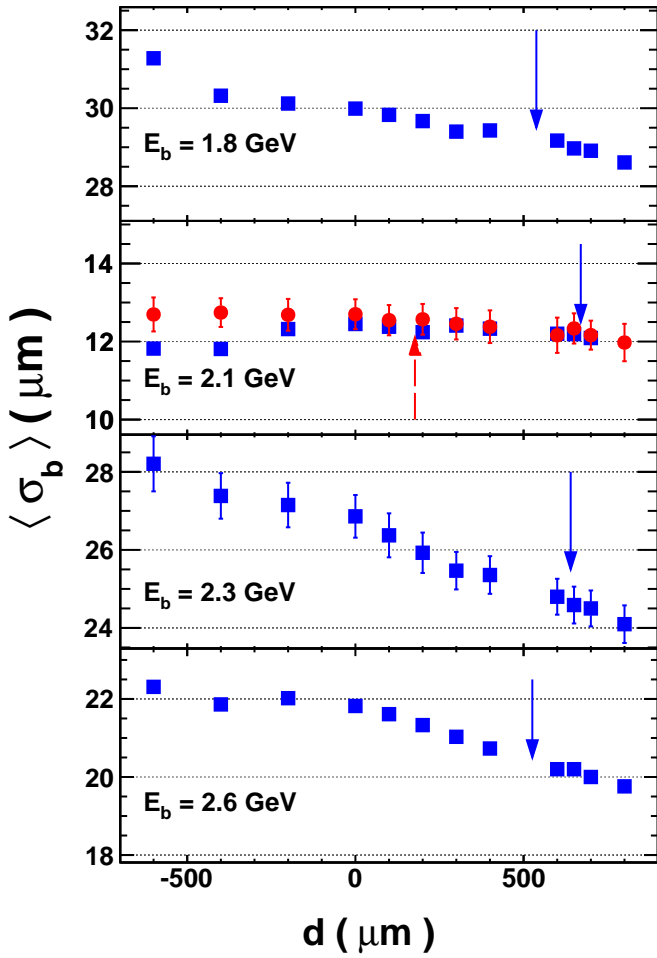


Figure 56: Turn-and-run-averaged σ_b for e^+ data image fits as a function of the detector offset, d , from the center of the pinhole that is used to generate templates, for four beam energies and five sets of beam conditions. The filled circles at $E_b = 2.1$ GeV are from a different set of beam conditions than the filled squares. Error bars indicate either statistical error from a single run (typically very small), or the standard error on the mean of several runs taken in the same beam conditions. Arrows indicate the minimum- χ^2/dof location according to the fits, as shown in Fig. 54; dashed upward arrow applies to filled circles, solid downward arrows to filled squares.

in Sect. 5.1 by fixing certain of the points to extremes of their error bars and refitting. None of these spectral response functions, shown in Fig. 57, can be excluded by more than one standard deviation as being closer to reality than the nominal one. Both coded aperture (with no filter) and pinhole (with the diamond filter) data were analyzed using `prfs` from these alternate spectral responses. The extreme variations from nominal were obtained for spectra applied to CA1 data from curves #1 and #6, giving beam sizes that were $\sim 0.35 \mu\text{m}$ below and above the nominal result, respectively. For PH data, the extremes were obtained from curves #6 and #7, giving beam sizes that are $\sim 0.5 \mu\text{m}$ smaller and larger, respectively, than the nominal PH run-and-turn-averaged beam size. We use these extremes as estimates of systematic uncertainty, which apply only to the no-filter (NF) and diamond-filter (Di) data, for which a broad spectrum is sampled.

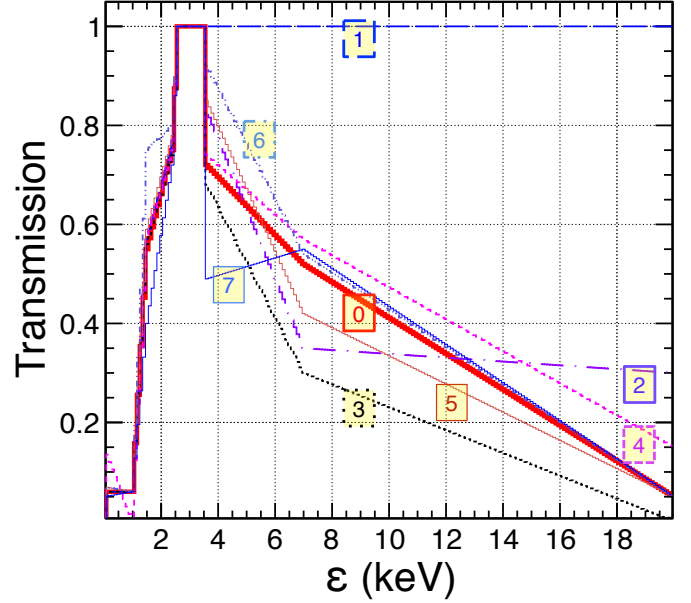


Figure 57: Spectral response curves used to explore sensitivity of measured beam size to the detected x-ray spectrum. The thickest solid curve represents the nominal spectrum and is labeled as “0”; seven other alternative responses are also shown and labeled with numbers from 1-7.

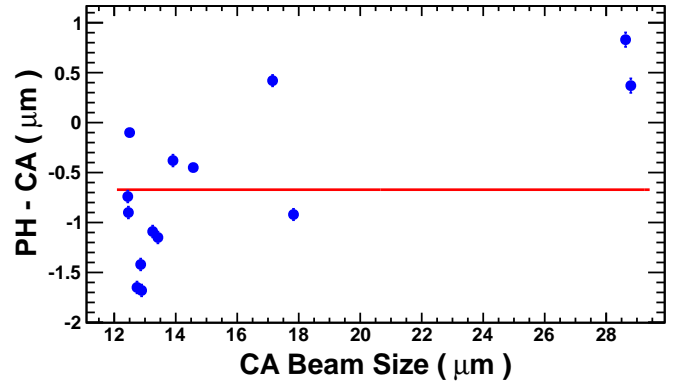


Figure 58: Difference between measured beam sizes as determined by the pinhole (PH) optic using the diamond filter and a coded aperture (CA1) using no filter vs. the CA1-determined beam size for a selection of CESR settings which result in a range of beam sizes. The solid horizontal line represents the mean difference in beam size.

5.4.8. Data-to-data comparisons

A comparison of data using CA1 with no filter to PH with the diamond filter at $E_b = 2.1$ GeV appears in Fig. 58. For this CESR fill, steering parameters were varied to sample a range of vertical beam sizes, from 12-30 μm . At each setting, data from CA1 and the PH were obtained, and so can be directly compared. Variations with beam size are too small to consider significant, given run-to-run variations. The overall average difference is of similar magnitude as the NF-Di difference observed for the PH optic alone in Fig. 50.

Finally, a comparison of beam sizes obtained with different filters at different beam energies, and with the two optical elements are shown in Fig. 59. Agreement is generally good, given known $\sim 1 \mu\text{m}$ variations in beam size during a run (the points

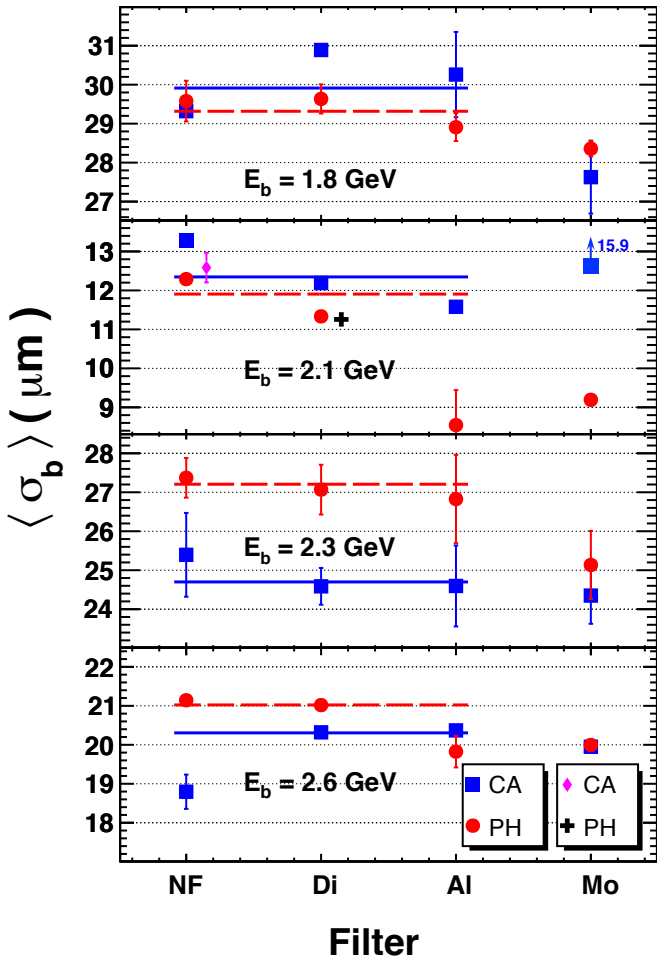


Figure 59: Turn-and-run-averaged σ_b for e^+ data image fits as a function of optical element and filter, for four beam energies and five sets of beam conditions. Circles represent results taken with the pinhole (PH) optic, and solid squares those taken with coded aperture CA1. A second dataset at $E_b = 2.1$ GeV is shown: the diamond represents use of CA1 with NF, and the cross applies to the PH optic with the Di filter. Horizontal lines represent fits to three filter (NF, Di, Al) points for CA1 (solid for squares) and PH (dashed for circles) results.

with small error bars include only one run with 1024 turns). Data from the molybdenum filter varies most in extracted beam size; this is perhaps not surprising given that it selects only a narrow part of the available spectrum, throwing away $\sim 90\%$ of the light relative to the no-filter (NF) setting.

5.4.9. Summary

A summary of expected systematic uncertainties appears in Table 7, where the uncertainties are listed at one energy and beam size, namely, $E_b = 2.1$ GeV and $\sigma_b \approx 12 \mu\text{m}$, and apply only to the broad-spectrum filter data (NF and Di). Note that these uncertainties assume that the prf applied has been generated with the optimal parameters, including geometry, partially absorptive material, pinhole opening or slit sizes, and that for CA1 the optimal detector offset d is used, as described in Sect. 5.4.6. Uncertainties can be much larger if any of these is not the case. Note also that for PH data it assumes that the PH gap size is both known to within $\pm 2 \mu\text{m}$ and set at a size within

Table 7: Estimated systematic uncertainties in measured beam size (in μm), and their quadrature sums, for $\sigma_b \approx 12.0 \mu\text{m}$ and $E_b = 2.1$ GeV, as measured using no filter (NF) or the diamond filter (Di), of the pinhole (PH) and coded aperture (CA1) optical elements, listed by their characteristics P , for which variations ΔP away from nominal induce beam size uncertainty.

Characteristic P	ΔP	PH	CA1
Pinhole gap size	$2.0 \mu\text{m}$	0.60	-
Pinhole lip width	$2 \mu\text{m}$	1.33	-
Etched slit size	$0.5 \mu\text{m}$	-	0.28
Au mask thickness	$0.02 \mu\text{m}$	-	0.40
Optic vertical alignment	$44 \mu\text{m}$	~ 0	0.30
X-ray spectrum	-	0.50	0.35
Magnification	0.1%	0.01	0.03
Quadrature sum	-	1.54	0.67

$5 \mu\text{m}$ of that which would give the narrowest prf at that beam energy and filter setting; setting the opening $15 \mu\text{m}$ smaller than optimal increases the uncertainty five-fold. This uncertainty on beam size is expected to scale approximately as $\propto 1/\sigma_b$ and $\propto 1/E_b$, with the exception of the effect of magnification uncertainty, which scales as σ_b . Taking the total uncertainties in quadrature can account for observed systematic differences between PH and CA1 results of $\sim 1.6 \mu\text{m}$ at this beam energy and beam size, as shown in Fig. 58.

The foregoing analysis demonstrates that $\sim 1 \mu\text{m}$ precision on beam size can be attained with the xBSM, but only after acquiring detailed understanding of geometry, alignment, design and modeling of optical elements, detector calibration and spectral response, and effective operational procedures.

5.5. Bunch Oscillations

Turn-by-turn measurements occupy the time domain, but can be displayed in the frequency domain via a discrete Fourier transform. Because each turn represents a time interval of $2.56 \mu\text{s}$ at CESR, the frequency domain is $[0, 390.6]$ kHz, for which the result is symmetric about $(390.6/2)$ kHz and higher frequencies are mapped into this interval as harmonics. The intensity at each frequency is commonly referred to as the power and expressed in dB, relative to an arbitrary reference value. Because beam oscillations at CESR are generally above half-integer the convention is to plot only in $[390.6/2, 390.6]$ kHz, with the property that any frequency f below this range is mapped to an observed frequency $390.6 \text{ kHz} - f$. If there are N_t turns of data in the time domain, the bin size in the frequency domain is $390.6 \text{ kHz}/N_t$.

Three quantities measured by the xBSM lend themselves to frequency analysis: vertical beam position, vertical beam size, and image intensity. The interpretation of oscillations in image intensity is ambiguous; it could indicate vertical, horizontal, and/or longitudinal beam oscillations. Vertical intensity oscillations will occur due to the Gaussian profile in vertical angle of the synchrotron radiation and because for large vertical excursions the image can move partially or completely off the detector. Horizontal excursions of the beam relative to the nominal

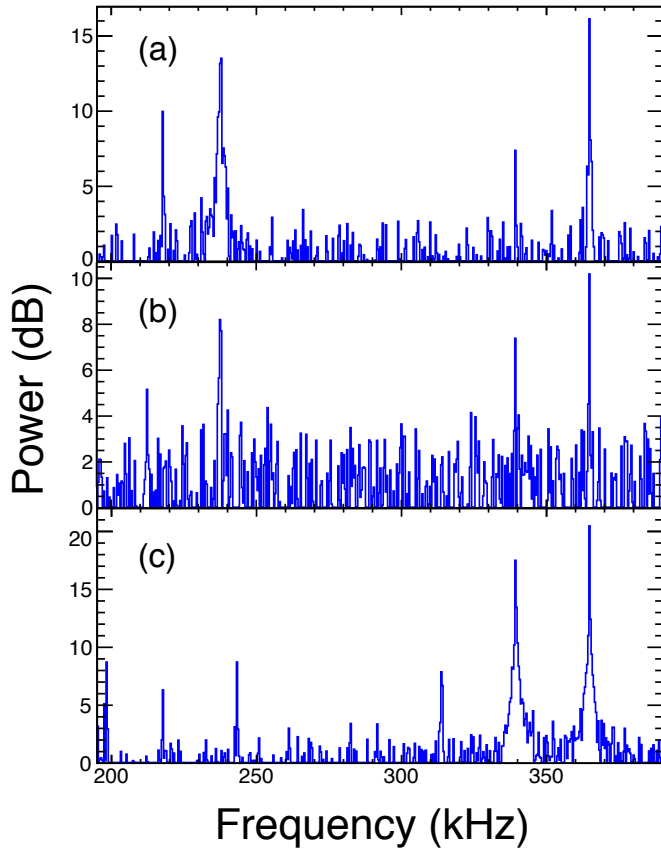


Figure 60: Fourier transforms of measured (a) vertical beam position, (b) vertical beam size, and (c) intensity of the image for an e^+ bunch at $E_b = 2.1$ GeV roughly in the middle of train of 30 bunches spaced by 4 ns. For reference for this data set the horizontal, vertical and synchrotron tunes were 227, 243, and 25 kHz, respectively, with the synchrotron dipole and quadrupole tunes visible as peaks at 365 and 340 kHz, respectively. The revolution frequency of CESR is 390.6 kHz.

orbit could result in some of the synchrotron radiation being blocked by one or more apertures; the width in the horizontal plane of the aperture at the optical element is ~ 1 mm at ~ 4.4 m from the source point. Longitudinal oscillations could not only couple with lateral oscillations, changing the direction of the emitted radiation, but also move the arrival time of the radiation away from the timing synchronization point, thus reducing recorded pulse height.

Fig. 60 shows these three quantities for data acquired with the pinhole optical element at $E_b = 2.1$ GeV and 1024 turns. Such measurements are critical for electron cloud beam dynamics studies.

5.6. Multi-bunch performance

Dynamics of multi-bunch running with short intervals between bunches is of substantial interest, in order to learn how to maintain bunch properties for all bunches in a train despite multi-bunch instability effects due to the electron cloud buildup for positrons. For example, Fig. 61 shows beam size as a function of bunch number for 30 bunches with 4 ns spacing, preceded by a *precursor* bunch 20 ns ahead of the train; without the precursor bunch, which is meant to temporarily sweep away the

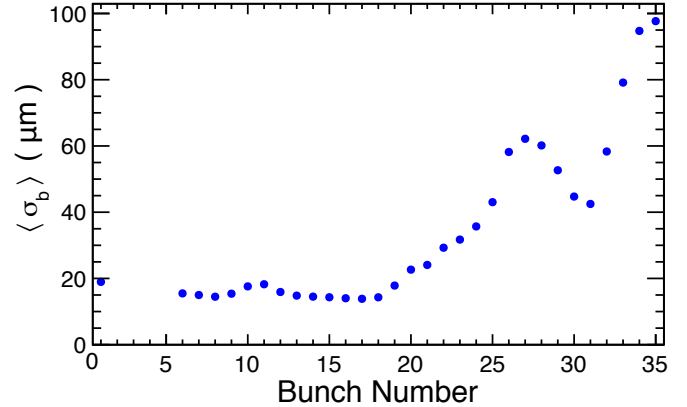


Figure 61: Turn-averaged beam size by bunch number for a run with 30 bunches in a train with 4 ns bunch separation and an additional precursor bunch 20 ns ahead of the train.

electron cloud, bunch #6 tends to have larger beam size. One of the goals of multi-bunch studies is to understand the bunch size increase at and after the sixteenth bunch and the effects of various spacings of precursor bunches on the beam size of the first bunch in the train. The frequency-domain quantities described in Sect. 5.5 are well-matched to study these phenomena. Fig. 62 shows the position, size, and intensity oscillations by bunch number. Beam size blow-up is correlated with introduction of oscillations in all three quantities at known beam oscillation frequencies. The xBSM is, by design, uniquely suited to analyze these behaviors under a variety of conditions.

6. Conclusions

We have described successful installation and operation of e^\pm x-ray beam size monitors (xBSM) for CESR-TA. The xBSM uses synchrotron radiation from a hard bend magnet as the light source. For $E_b \approx 2$ GeV, the xBSM images x-rays of $\epsilon \approx 1$ -10 keV ($\lambda \approx 0.1 - 1$ nm) onto a photodiode array. The xBSM has measured single-shot vertical beam sizes from 10-100 μm with absolute systematic uncertainty of $\pm 1 \mu\text{m}$. Single-shot performance holds down to 0.1 mA/bunch and 4 ns bunch separation. Acquiring and analyzing xBSM data of high quality has benefited from several lessons learned during development of the project. Having the detector and optics share the CESR vacuum has allowed windowless operation, extending the operational ranges of beam energy and beam current downward. Several startup protocols have proved to be essential for ensuring reliable operation, including geometrical scans of pinhole opening; positions of detector, optical element, and filter elements; timing scans of the electronics; and real-time adjustment of e^\pm orbits. Calibrations of the detector electronics in pulse height and bunch-to-bunch crosstalk were routinely acquired and utilized in order to properly interpret the data. Precision measurements of beam size and oscillations were obtained only after development of extensive analysis machinery to calibrate the apparatus, model geometrical and spectral response, and fit bunch-by-bunch, turn-by-turn beam crossing data using different optical elements and spectral filters. Study

of beam-size resolving-power has improved our ability to optimize pinhole openings and coded aperture patterns for best performance. The xBSM has already enabled important investigations of beam dynamics, including electron cloud studies [46], intra-beam scattering [47], low-emittance tuning [48], and horizontal crabbing [49]. Future development will include development of more effective optical elements, measuring performance up to ~ 5 GeV, and further work aimed toward making the device a real-time or nearly real-time machine-tuning tool.

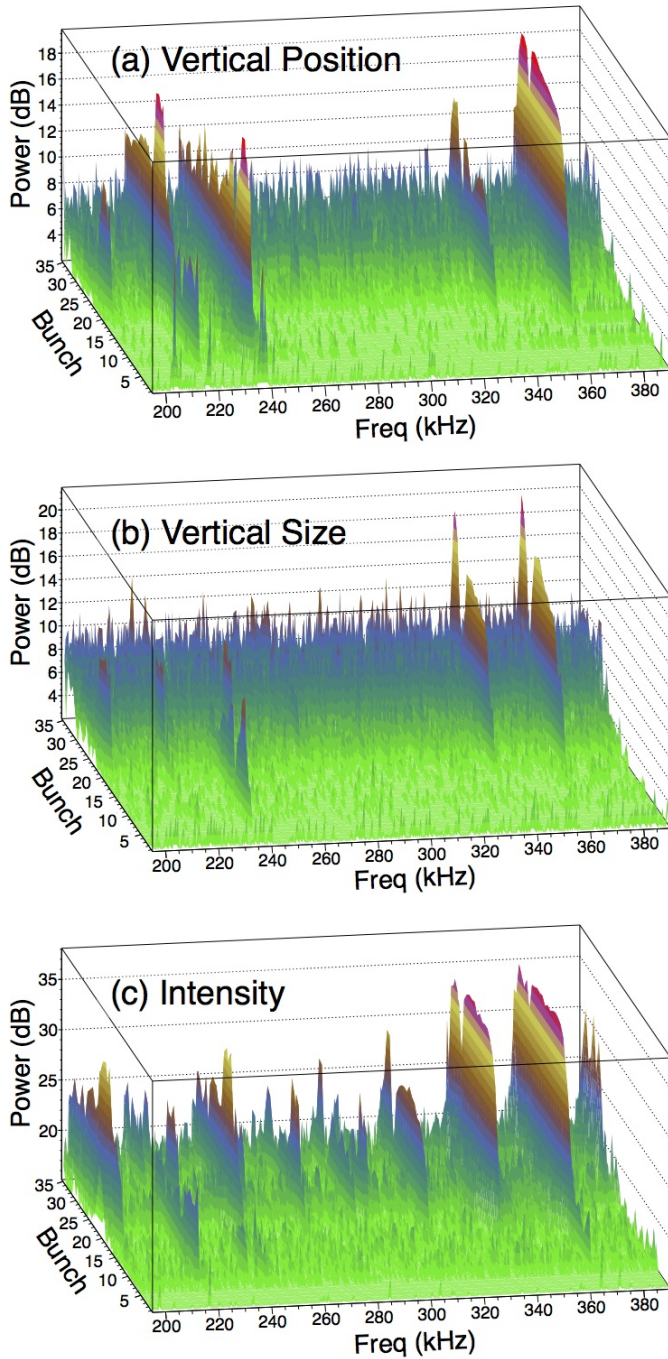


Figure 62: Fourier transforms, by bunch number, of measured (a) vertical beam position, (b) vertical beam size, and (c) intensity of the image.

Acknowledgments

This work would not have been possible without the meticulous efforts of the CESR Operations Group and support of the Cornell Laboratory for Accelerator-based Sciences and Education (CLASSE) and Cornell High Energy Synchrotron Source (CHESS). This research was supported under the National Science Foundation awards PHY-0734867, PHY-1002467, PHYS-1068662, Department of Energy contracts DE-FC02-08ER41538 and DE-SC0006505, and by the NSF and National Institutes of Health/National Institute of General Medical Sciences under NSF award DMR-0936384.

The authors thank M. Billing, N. Eggert, B. Kreis, H. Liu, M. McDonald, and M. Palmer for their participation in and contributions to the xBSM project.

References

- [1] J. W. Flanagan, Conf. Proc. C **110904** (2011) 1959 ([link](#)).
- [2] Z. Dolezal (for the Belle Collaboration), PoS EPS **-HEP2009** (2009) 143; [arXiv:0910.0388 \[hep-ex\]](#).
- [3] V. N. Litvinenko *et al.*, ICFB Beam Dyn. Newslett. **58** (2012) 52; [arXiv:1109.2819 \[physics.acc-ph\]](#).
- [4] M. Borland, Conf. Proc. C **1205201** (2012) 1035 ([link](#)).
- [5] <http://www.lightsources.org/regions>
- [6] Y. Cai *et al.*, Phys. Rev. ST Accel. Beams **15** (2012) 054002 ([link](#)).
- [7] Global Design Effort, *THE INTERNATIONAL LINEAR COLLIDER: Technical Design Report*, (2013) ([link](#)).
- [8] Y. Papaphilippou *et al.*, Conf. Proc. C **1205201** (2012) 1368 ([link](#)).
- [9] A. S. Aryshev *et al.*, Conf. Proc. C **110904** (2011) 1964 ([link](#)).
- [10] A. S. Aryshev *et al.*, Jour. of Phys.: Conf. Series **236** (2010) 012008 ([link](#)).
- [11] P. Karataev *et al.*, Nucl. Instrum. Meth. B **227** (2005) 158 ([link](#)).
- [12] L. Bobb *et al.*, Proceedings of IBIC2012, Tsukuba, Japan, (2012) 24 (MOCC01) ([link](#)).
- [13] T. Aumeyr *et al.*, Proceedings of IPAC2013, Shanghai, China (2013) 789 (MOPWA051) ([link](#)).
- [14] H. Ikeda *et al.*, Conf. Proc. C **0505161** (2005) 3194 ([link](#)).
- [15] T. Mitsuhashi, Proc. School on Particle Accelerators, Beam Measurement; World Scientific, Singapore, (1998) 399.
- [16] T. Naito and T. Mitsuhashi, Conf. Proc. C **060626** (2006) 1142 (TUPCH058) ([link](#)).
- [17] T. Naito and T. Mitsuhashi, Conf. Proc. C **100523** (2010) 972 (MOPE009) ([link](#)).
- [18] Å. Andersson *et al.*, Nucl. Instrum. Meth. A **591** (2008) 437 ([link](#)).
- [19] P. Elleaume *et al.*, J. Synchrotron Rad. **2** (1995) 209 ([link](#)).
- [20] F. Ewald *et al.*, Proc. DIPAC2011 (2011) 188 (MOPD61) ([link](#)).
- [21] C. Thomas *et al.*, Phys. Rev. ST Accel. Beams **13** (2010) 022805 ([link](#)).
- [22] T. Weitekamp *et al.*, Nucl. Instrum. Meth. A **467** (2001) 248 ([link](#)).
- [23] S. N. Nakamura *et al.*, Conf. Proc. C **030512** (2003) 530 ([link](#)).
- [24] H. Sakai *et al.*, Phys. Rev. ST Accel. Beams **10** (2007) 042801 ([link](#)).
- [25] Y. S. Chu *et al.*, Appl. Phys. Lett. **92** (2008) 103119 ([link](#)).
- [26] R. Klein *et al.*, Conf. Proc. C **110904** (2011) 1165 ([link](#)).
- [27] R. F. Campbell *et al.*, Conf. Proc. C **1205201** (2012) 2081 (WEYA02); ([link](#)).
- [28] J. Larmor, Phil. Trans. Roy. Soc. London **190A** (1897) 205; *Aether and Matter*, Cambridge University Press (1900); Philos. Mag. **44**(S.5) (1897) 503.
- [29] A. Liénard, L'Éclairage Électrique 16 pp5 53 (1898) 106.
- [30] E. Wiechert, Archives Néland (2)5 (1900) 45; Ann. Phys. **309** (1901) 667.
- [31] G. A. Schott, Philos. Mag. **13** (1907) 189; *Electromagnetic Radiation*, Cambridge University Press (1912).
- [32] J. Schwinger, Phys. Rev. **75** (1949) 1912 ([link](#)).
- [33] J. D. Jackson, *Classical Electrodynamics* (Second Edition), John Wiley & Sons (1975).
- [34] B. L. Henke, E. M. Gullikson and J. C. Davis, Atom. Data Nucl. Data Tabl. **54** (1993) 181; updated tables available from henke.lbl.gov/optical_constants/asf.html
- [35] ROOT version 5.34/02, R. Brun and F. Rademakers, Nucl. Instrum. Meth. A **389** (1997) 81 ([link](#)). See also root.cern.ch.
- [36] MATLAB® version 7.10.0. Natick, Massachusetts: The MathWorks Inc., 2010.
- [37] FFTW version 3.3, M. Frigo and S. G. Johnson, Proc. IEEE **93** (2) (2005) 216. www.fftw.org
- [38] MINUIT: root.cern.ch/root/html/TMinuit.html
- [39] R. H. Dicke, Astrophys. Journ. **153** (1968) L101 ([link](#)).
- [40] E. E. Fenimore and T. M. Cannon, Appl. Optics **17** (1978) 337.
- [41] www.chess.cornell.edu.
- [42] Fermionics Opto-Technology, Inc., 4555 Runway St., Simi Valley, CA 93063 USA, www.fermionics.com
- [43] Applied NanoTools, Inc. #1200 - 10045 111 Street, Edmonton, Alberta T5K 2M5, CANADA, www.appliednt.com
- [44] M. Arinaga *et al.*, Proceedings of IBIC2012, Tsukuba, Japan, (2012) 6 (MOCB01) ([link](#)).
- [45] J. W. Flanagan *et al.*, Proceedings of IBIC2013, Oxford, UK, 16-19 Sep. 2013, WEPF15 (2013). ([link](#)).
- [46] G. Dugan *et al.*, CERN Yellow Report CERN-2013-002, pp.31-41 [[arXiv:1310.0261 \[physics.acc-ph\]](#)].
- [47] M. P. Ehrlichman *et al.*, Phys. Rev. ST Accel. Beams **16** (2013) 104401 ([link](#)), [[arXiv:1308.0035 \[physics.acc-ph\]](#)].
- [48] J. Shanks, D. Rubin, and D. Sagan, [arXiv:1309.2247 \[physics.acc-ph\]](#).
- [49] M. P. Ehrlichman *et al.*, [arXiv:1311.1763 \[physics.acc-ph\]](#).